NOVA SCHOOL OF SCIENCE & TECHNOLOGY

DEPARTAMENT OF PHYSICS

RODRIGO DIAS SANTOS

BSc in Physics Engineering

# FREE-SPACE OPTICAL COMMUNICATION: DEVELOPMENT OF A POINTING, ACQUISITION AND TRACKING SYSTEM

## SPECIFICATIONS DESIGN, SYSTEM SIMULATION

MASTER IN PHYSICS ENGINEERING

NOVA University Lisbon

September, 2024

NOVA SCHOOL OF SCIENCE & TECHNOLOGY

DEPARTAMENT OF PHYSICS

# FREE-SPACE OPTICAL COMMUNICATION: DEVELOPMENT OF A POINTING, ACQUISITION AND TRACKING SYSTEM

## SPECIFICATIONS DESIGN, SYSTEM SIMULATION

**RODRIGO DIAS SANTOS**

BSc in Physics Engineering

**Adviser:** Raquel Cardoso Henriques
Optical Technical Manager, Lusospace

**Co-advisers:** Pedro Manuel Cardoso Vieira
Assistant Professor, FCT-NOVA

**Examination Committee:**

**Chair:** André João Maurício Leitão do Valle Wemans,
Assistant Professor, FCT-NOVA

**Rapporteurs:** Paulo António Martins Ferreira Ribeiro,
Associate Professor, FCT-NOVA

**Adviser:** Raquel Henriques
Optical Technical Manager, Lusospace

MASTER IN Physics Engineering

NOVA University Lisbon
September, 2024

**Free-Space Optical Communications:**
**Development of a Pointing, Acquisition, and Tracking System**

Dedico à minha família e principalmente aos que fizeram de mim o "Cientista" e "Santola-Man" de hoje. Pelos transformadores de alta tensão, pelos condensadores, extintores e até cursos informais de soldadura...

Aos meus tios Rui, Serafim e Isidro.

# ACKNOWLEDGMENTS

Quero começar por agradecer à Lusospace pela oportunidade de trabalhar com eles nesta tese. Um agradecimento especial ao Ivo pela oportunidade de poder exercer engenharia a este nível em Portugal. Quero por outro lado agradecer a todos os "Lusonautas", com especial ênfase à minha orientadora Raquel. Foi ela quem aturou todas as minhas questões, delírios e ideias com toda a paciência e empatia. Quero também agradecer ao meu coorientador Pedro Vieira por ter aceitado ser parte desta tese e por estar sempre disponível para todas as minhas curiosidades.

Naturalmente, não podia deixar de agradecer à FCT, e especialmente ao curso de MIEF. Um obrigado especial aos meus Padrinhos Marley e Rúben, tal como às minhas pequeninas Mariana, Sara e Inês. Mas em boa verdade quero agradecer acima de tudo ao BANG, pela amizade mais genuína e de preocupação que podia existir. O meu obrigado ao Fon, Babs, Minnie, Grab, Ana e Maggy. "*This is the end of beggining*"

Obrigado, "*JPManso*", "*Vieira_in*", "*Arruaceiros*", "*Os_que_viram_o_filme/rs*" por estarem comigo em todas as felicidades e tristezas. São vocês que marcam o que melhor levo em todas as fases da minha vida. Não posso deixar de agradecer à minha Bea por me acompanhar e suportar nesta fase tão importante.

Obrigado a todos os professores que me fizeram chegar aqui com especial ênfase ao Gonçalo Oliveira. Foram vocês o motor da minha curiosidade que me levou a este "mundo".
Finalmente quero agradecer a toda a minha família, mas principalmente à Fernanda, Américo, Sofia e Diogo. Sem vocês era impossível estar onde estou hoje... OBRIGADO!

"Everything should be made as simple as possible, but not simpler" (Einstein).

# ABSTRACT

The present thesis is an integral subsystem of a Lusospace project, which encompasses the design and conceptual validation of a Pointing, Acquisition, and Tracking (PAT) system. This system will integrate into a low-profile Optical Head (OH) terminal for airborne-to-spacecraft communications. The PAT system bears the responsibility of signal acquisition and ensuring optical alignment between both terminals to uphold communication stability.

The document starts by providing the project context and introducing the pertinent background theory that underpins the system's design. A review of the current state of the art follows, highlighting the significance of the work within the broader scope of Free-Space Optical Communications (FSOC). Following this, the PAT architecture is described in accordance with the international protocol SDA. [1] The thesis then presents the components involved, their functions, and their specifications, which directly determine the PAT budget across the multiple PAT phases.

Finally, a numerical model design is outlined, considering the different budgets as inputs. The presented thesis ultimately shows how the system's design meets the imposed requirements. In conclusion, the critical parameters for the well-functioning of the system are compliant. Some other parameters lack further study. This work contributes not only to Lusospace's project but also to the wider development of Free-Space Optical Communications (FSOC).

**Keywords**: Pointing, Acquisition and Tracking; Optical Head; Budget, Numerical Model, Free-Space Optical Communications

# RESUMO

Esta tese representa parte de um projeto da Lusospace que compreende o desenvolvimento e validação conceptual de um sistema de Pointing, Acquisition and Tracking. (PAT) Este sistema será integrado num terminal de um Optical Head, (OH) de baixo perfil, para comunicações entre aeronaves e satélites. O sistema PAT é responsável por adquirir o sinal do satélite e por garantir o alinhamento entre ambos os percursos óticos, assegurando a estabilidade da comunicação.

O documento começa por fornecer o contexto do projeto e introduzir a teoria relevante para o design do sistema. De seguida, o estado de arte é apresentado, destacando a relevância do trabalho desenvolvido nesta tese. Depois disso, a arquitetura do sistema PAT é descrita de acordo com o protocolo internacional SDA. [1] Posteriormente, os componentes envolvidos bem como as suas funções são descritos, devidamente. Como consequência das especificações selecionadas, o PAT budget converte as mesmas especificações para contribuições que afetam o funcionamento do sistema. (PAT budget)

Por fim, é delineado um modelo numérico que toma em conta as várias incertezas. Este modelo numérico permite aferir se o design do sistema cumpre os requisitos estabelecidos, previamente. Em suma, os requisitos críticos para o funcionamento do sistema são cumpridos. Por outro lado, outros carecem de um estudo mais profundo. Este trabalho contribui não só para o projeto da Lusospace, mas também para o desenvolvimento mais amplo do ramo de comunicações óticas. (FSOC)

**Palavras chave:** Pointing, Acquisition and Tracking; Optical Head; Budget, Modelo Numérico, Comunicações Óticas em espaço-livre

# CONTENTS

# LIST OF FIGURES

# List of Tables

# GLOSSARY

| | |
|---|---|
| **Uncertainty Budget** | Table of itemizable components that contribute to the uncertainty of a system |
| **Lead** | Terminal responsible for initiating the acquisition process. (Aircraft) |
| **Follow** | Satellite |
| **Radome** | Structural weatherproof structure, which protects communication terminals |

# ACRONYMS

| | |
|---|---|
| **ARTES** | Advanced Research in Telecommunications Systems |
| **ATS** | Acquisition, Tracking Sensor |
| **A.U.** | Arbitrary Units |
| **A/C** | Aircraft |
| **CPM** | Coarse Pointing Mechanism |
| **ESA** | European Space Agency |
| **FFOV** | Full Field Of View |
| **FOU** | Field of Uncertainty |
| **FOV** | Field Of View |
| **FPA** | Fine Pointing Acquisition |
| **FSM** | Fast Steering Mirror |
| **FSOC** | Free-Space Optical Communications |
| **GEO** | Geosynchronous Equatorial Orbit |
| **GNSS** | Global Navigation Satellite System |
| **HFOV** | Half Field Of View |
| **INS** | Inertial Navigation System |
| **LoS** | Line of Sight |
| **MEMS** | Micro-Electromechanical Systems |

| | |
|---|---|
| **MEO** | Middle Earth Orbit |
| **OC** | Optical Communication |
| **OH** | Optical Head |
| **PAA** | Point Ahead Angle |
| **PAT** | Pointing, Acquisition, Tracking |
| **PAM** | Point Ahead Mechanism |
| **OP** | Optical Path |
| **SDA** | Space Development Agency |
| **S/C** | Spacecraft |

# SYMBOLS

| | |
|---|---|
| $r_s$ | Distance from the scanning point to the scan's centre |
| $\theta_s$ | Angle of the scanning point |
| $L_\theta$ | Step Factor |
| $\theta_{div}$ | Beacon Divergence |
| $F_o$ | Overlap Factor |
| $T_{dwell}$ | Dwell Time |
| $T_r$ | Response Time |
| $c$ | Speed Light |

# 1

# INTRODUCTION

Satellite communications represent a significant segment within the space industry. Therefore, the European Space Agency (ESA) launched a broad program to compete in this market. Advanced Research in Telecommunications Systems (ARTES) program aims to lead the industry in this sector.

Until today, most communications between aircraft and other objects were performed predominantly through radio frequency, resulting in a low data rate and susceptibility to interception by third parties due to electromagnetic wave spreading. Optical Communications (OC) overcome these problems. Leveraging the higher bandwidth of the optical spectrum, they offer the possibility of modulating more information into these channels. Moreover, OC enhances higher security since the transmission and reception of the signal are performed in Line of Sight (LoS). This naturally reduces the possibility of intercepting the signal. However, achieving this goal presents numerous challenges.

Within this context, the European Space Agency (ESA) launched a sub-programme inside the ARTES program called Scylight (pronounced Skylight). This strategic schedule intends to address and stimulate the development of optical and quantum technologies for satellite communications.

Although some technologies exist for OC between aircraft (A/C) and spacecraft (S/C), very few to none have a low-profile structure. Therefore, as part of this initiative, ESA proposed several ideas, one of which was to create a low-profile Optical Head (OH).

Lusospace took a significant step in pursuing this idea by launching a dedicated project to achieve a proof of concept for this product. This concept sets the basis for developing a terminal for airborne OC, specifically for commercial aircrafts. This project will bring many advancements in establishing inflight OC with satellites in the Middle Earth Orbit (MEO) altitude.

However, one of the main technical challenges in achieving this vision is the alignment of both optical paths, which represents a significant hurdle in establishing OC between A/C and S/C. The cumulative uncertainties of all optical, electronic, and mechanical components impede the terminal from reaching direct and instantaneous communication. To mitigate this problem, the optical terminal must have a Pointing, Acquisition, and Tracking (PAT) system.

The PAT system comprises three fundamental stages. The first is the pointing phase, which occurs when the OH points the beacon towards the most probable position of the satellite. In the second phase, the terminal performs a scan within a range of angles defined by its Field of Uncertainty. (FOU) This stage may also include some other alignments. After establishing LoS contact with the satellite, the airborne terminal transitions to a tracking phase. This last one aims to align both optical paths and to accommodate all the vibrations and errors inherent to the system. This final stage ensures communication stability.

## 1.1 Goal

The aim of this thesis centres around crafting the OC terminal's PAT system specifications. To achieve that, the PAT budget is meticulously designed by analysing the multiple contributions and component specifications.

Secondly, this thesis aims to build a PAT "emulator" from scratch. This numerical model shall receive as inputs the designed budgets, referred to above. The PAT emulator encompasses statistics from the multiple stages of the system starting in the pointing phase until the success and stability communication analysis.

In the end, a performance study is done to evaluate the system objectively. The resultant data from the emulator is properly analysed, enabling the compliance assessment of the multiple requirements defined in a previous stage of this project.

The research work described in this dissertation was carried out in accordance with the norms established in the ethics code of Universidade Nova de Lisboa. The work described and the material presented in this dissertation, with the exceptions clearly indicated, constitute original work carried out by the author.

# 2

# THEORETICAL BACKGROUND

This chapter explores the basic aspects of generic PAT systems. Each subsection introduces the key subsystems and their function in ensuring effective communication. By the end, the reader will have a clear understanding of the multiple phases involved in a PAT system and the different approaches that can be taken to achieve optimal performance.

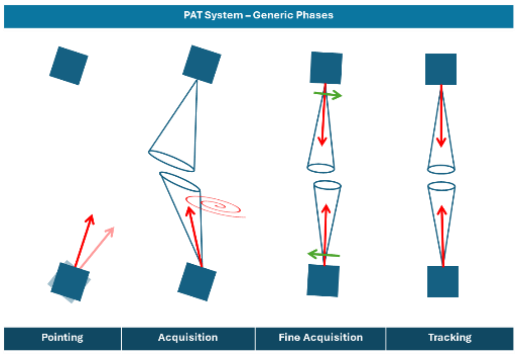


Figure 2.1 - PAT system generic phases

## 2.1 Pointing phase

The pointing phase is defined by the moment in which the OH redirects its beacon to the most probable point of the satellite's signal acquisition. This stage demands measurements of the aircraft's attitude and position (acquired by a GNSS/INS system). By combining this dataset with the movement data of the target satellite (Ephemeris data), the necessary actuation parameters for all the gimbals in the Coarse Pointing Mechanism (CPM) are determined. This phase is concluded once the CPM is fully directed towards the pointing goal.

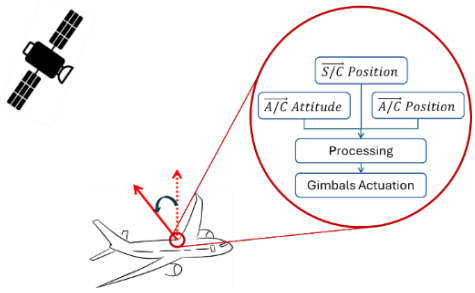


Figure 2.2 - Pointing phase illustration

## 2.2 Acquisition phase

After directing the beacon to the pointing goal, the acquisition phase will use the same ephemeris data and CPM to perform a scan of a given angle's interval (there are also different approaches, although this is the most reliable one). The gimbals will change their angles (azimuth and elevation) so that the whole uncertainty cone (or FOU) is scanned, also accounting for the relative speed between both A/C and S/C.

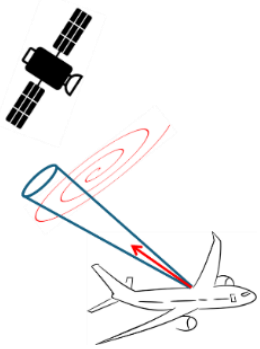

Figure 2.3 - Acquisition phase illustration; Blue cone - Terminal FOV; Red arrow - Beacon direction

### 2.2.1 Field of Uncertainty (FOU)

The chosen Field of Uncertainty (FOU) determines the angles' interval to be analysed and, therefore the theoretical probability of establishing LoS contact with the satellite. This same FOU (Figure 2.4) is always determined relative to the sum of the uncertainty contributions, known as the open-loop acquisition pointing uncertainty. (more details in Chapter 6).

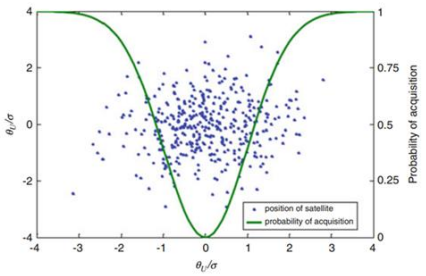


Figure 2.4 - Acquisition probability and satellite distribution representation [2];
Green - Acquisition probability in function of selected FOU; Blue - Satellite distribution scattered.;
$\theta_U/\sigma$- FOU relative to the open-loop acquisition pointing uncertainty

### 2.2.2 Acquisition approach

As mentioned previously, the acquisition phase involves scanning the uncertainty region. However, this stage can be achieved using different approaches. [2] In this project, it is assumed the lead to be the A/C and the follow the S/C [1], since the first is the one to initiate the communication attempt.

#### 2.2.2.1 Stare/Stare

This mode of acquiring the target's signal involves both lead and follow to be "staring" at each other. In other words, the lead has a beacon with beam divergency big enough to cover the chosen FOU. At the same time, the follow has a sensor that stays focused on the entire FOU, ready to receive a signal from any point within it.

This approach requires too much power to meet the required beacon brightness. Therefore, it is only suitable for short-range communication, which does not match the project requirements.

#### 2.2.2.2 Scan/Scan

Both systems scan each other until the LoS contact is established, using a low divergence beacon. This mode of acquisition should not be the first choice due to the increase in acquisition time, although it is suitable when one of the terminals has low pointing uncertainty.

#### 2.2.2.3 Scan/Stare

This case is one odd approach to acquisition. Here, the lead shines a divergent beam. At the same time, the follow FOV shall scan the uncertainty region until it finds the lead's source. This approach is not suitable for our application due to power requirements.

#### 2.2.2.4 Stare/Scan

In this case, the lead is responsible for scanning the follow's position. Simultaneously, the S/C stares within its FOV until it receives a signal from the transmitting terminal. This concept is ideal for the context of this project since it is low-power demanding. It still enables short acquisition times, even though longer than the "stare/stare" approach. Therefore, this is the chosen scanning approach.

### 2.2.3 Scanning patterns

There are multiple ways to scan a given space. The chosen scanning pattern is the continuous Spiral Scan (Figure 2.5 A). This pattern allows the CPM to scan the FOU from the highest acquisition probability point to the lowest one.

Nevertheless, there are also other scanning patterns, such as Step Spiral Scan (Figure 5 B), where the spiral is traced in straight lines, as the image below shows, offering a simpler movement but inducing more mechanical vibrations in the system due to the quick change in direction. The Segmented Scan (Figure 2.5 C) starts in the centre of the FOU. However, the area is broken into different segments. The Raster Scan (Figure 2.5 D) differs from the previous one since one of the axes is fully scanned while the other is incremented in steps. None of these scan patterns is statistically beneficial since they do not consider the probability density, which is highest in the centre of the scan and falls radially. Below, the characteristics of the chosen scanning pattern shall be presented. [2]

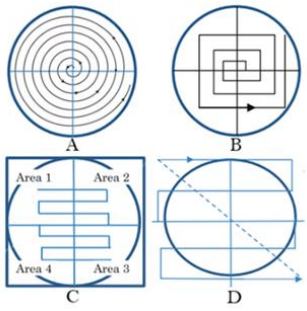


Figure 2.5 - Scanning patterns [2]

The continuous spiral scan starts in the centre of the space since it is usually where the acquisition probability is higher. After that, the search beacon performs a movement that the following parameterisation in polar coordinates can describe:

$$r_s = \frac{L_\theta}{2\pi} \times \theta_s \qquad 2.1$$

where $r_s$ is the distance from the scanning point to the centre of the FOU. $\theta_s$ is the angle of the scanning point. $L_\theta$ corresponds to the step factor and is described also by the formula:

$$L_\theta = \theta_{div} \times (1 - F_o) \quad 2.2$$

where $\theta_{div}$ corresponds to the divergence of the searching beacon and $F_o$ to the overlap factor. This overlap factor defines the distance between each turn (relative to the beacon divergence). Both variables described above bring us to an important balance that must be considered.

A more divergent beacon leads to a more significant step factor. Mathematically, a bigger spiral is obtained, which results in a faster acquisition for the same FOU. However, as discussed in the previous subsection, a large beacon divergence demands higher-power lasers. The opposite results in a more economical design and longer acquisition times.

From a different perspective, a higher overlap factor slows down the acquisition, although you scan the FOU with higher redundancy. This redundancy is useful if the pointing uncertainty (due to micro-vibrations and other contributors) is too high. (Chapter 6.1). On the other side, a lower overlap factor results in lower redundancy, which may reduce the acquisition probability.

Although a mathematical parameterisation of the trace scan is presented, this acquisition process must be discrete. The search shall be performed in iterations spaced by an iterative step (more information in Chapter 4). At each interval, the system must wait a specific time given by $T_{dwell}$. This will ensure that both sensors receive enough photons to detect the signal. The scan time will be given by:

$$T(r_s) \approx \frac{\pi {\theta_s}^2}{L_\theta^2} \times T_{dwell} \quad 2.3 \qquad T_{dwell} = T_R + 2\frac{R}{c} \quad 2.4$$

with $R$ being the distance between both objects and $c$ the speed of light. Additionally, response time ($T_R$) is added, due to the possible limitations in the actuation and sensing mechanisms and even the signal processing. [2], [3]

In practical terms, this theoretical approach leaves some problems to be solved, which will be discussed in the PAT system architecture Chapter 4.1 and PAT emulator Chapter 7.

## 2.3 Fine pointing acquisition and tracking phases

Once the acquisition phase is finished, the system transitions to a fine pointing acquisition phase. Here, the system must be able to align both optical path vectors and correct the

pointing errors until the signal enters the Rx FOV. Only then the system achieves communication and transitions to a tracking phase. This last one will correct the high-frequency vibrations during the entire communication period.

These two final stages of the PAT system require the implementation of a closed-feedback loop. Consequently, a measurement system is needed to quantify the error between the pointing goal and the real pointing direction. Multiple sensor configurations can perform these measurements, as described below.

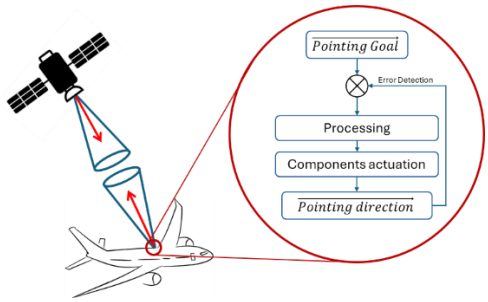


Figure 2.6 - Tracking phase; Blue cone - Terminal FOV; Red arrow - Beacon direction

## 2.3.1 Measurement configurations

### 2.3.1.1 Quadrant sensor

The first configuration involves a quadrant sensor, responsible for tracking the signal. The quadrant sensor uses a smaller active area divided into four circle quarters. This sensor is small enough for the beam section to cover all the quadrants. Therefore, the sensor detects the affected area by the photons in each quarter. Based on this information, the system estimates the necessary correction of the optical path vector. This sensor offers greater accuracy and faster data readouts, making it useful for sub-microradian errors with high-frequency bandwidth. An acquisition sensor is required to correct larger errors with smaller frequencies. This configuration makes this system highly reliable since the acquisition sensor may have a large FOV to ensure the satellite's acquisition. At the same time, the FOV of the quadrant sensor may be as small as intended, enabling high accuracy regarding the optical path alignment.

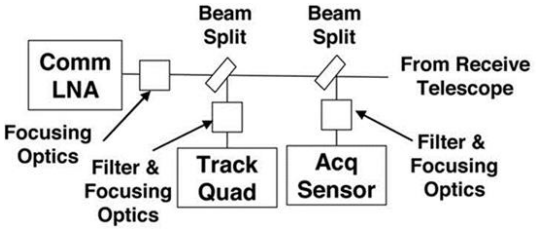


Figure 2.7 - Quadrant sensor configuration [3]

This configuration (Figure 2.7) requires more components in the system, which may result in increased complexity. Furthermore, more sensing components will decrease the input power in the communication sensor. [2], [4]

#### 2.3.1.2 Acquisition sensor subarray

The preferred configuration involves using a state-of-the-art sensor array (ATS) that can progressively deactivate its pixels. As a result, the sensor's readout rate increases, followed by a higher SNR (since fewer pixels result in smaller total noise). [3] This setup combines the benefits of the quadrant sensor and the acquisition sensor, reducing the number of system components needed.

However, this approach involves a trade-off. A larger FOV ensures the satellite's signal acquisition but reduces the tracking accuracy. Simultaneously, a lower FOV enhances higher accuracy in the tracking phase but makes the satellite acquisition more challenging.

Despite the increased alignment time drawback and the necessary trade-off, the improved efficiency and reduced complexity make this configuration (Figure 2.8) the preferred choice for this project.

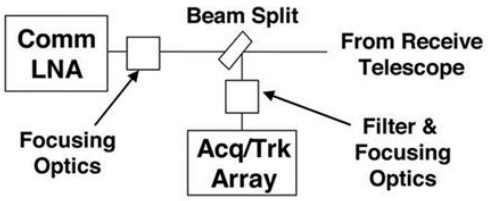


Figure 2.8 - ATS configuration [3]

### 2.3.2 Point Ahead Angle (PAA)

Due to limited light speed, the Point Ahead Mechanism (PAM) shall be employed in the emission of the transmitting laser. This mechanism will point the laser ahead based on the relative velocities of aircraft and spacecraft. The system achieves this correction using an offset mirror that points the beacon ahead. [3]

$$Point\ Ahead\ Angle\ (PAA) = \frac{2\,v}{c} \qquad 2.5$$

where $v$ is the relative velocity between both bodies and $c$ is the light speed. This formula can be proven through the equations found in Appendix A.

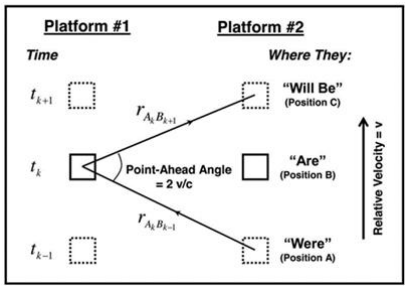


Figure 2.9 - Point ahead angle representation [3]

## 2.4 PAT protocol example

Bellow, it is presented all the stages of a specific PAT system (Figure 2.10). This diagram was taken from a standard protocol for FSOC. This system operates in a stare/scan mode. The system differs from the theory presented above in the fact that both lead and receiver scan each other alternately (acquisition 1A 1B - Figure 2.10).

The Space Development Agency (SDA) protocol represents a significant advancement in the OC field. While there are already many protocols for radiofrequency communication, OC lacks such protocols. This document fills this gap by defining the fundamentals of interoperability between optical systems. It details many aspects of OC, such as scanning methods, wave modulation, data rate, etc. This protocol lays the foundation for all forms of OC in space, ensuring consistent and reliable communication. [1]

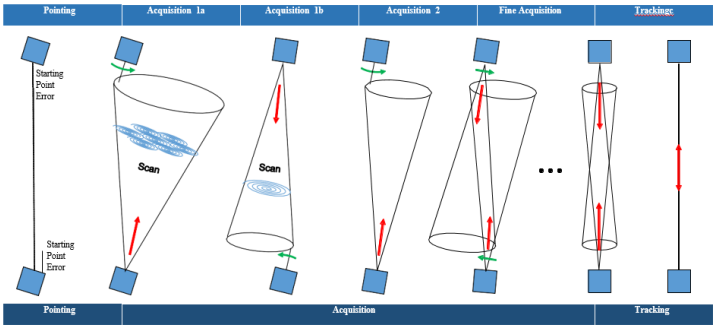


Figure 2.10 - Representative SDA (Stare/Scan approach) [1]

# 3

# STATE OF THE ART

Despite the increasing research in free-space optical communication, studies specifically focused on PAT systems remain limited. The most notable project was the LOLA programme (Figure 3.2) that achieved airborne OC with a Geosynchronous Equatorial Orbit (GEO) S/C for 20-minute periods, transmitting in the aircraft a famous live French show in HD quality. There was also a project in China (Figure 3.1) that performed OC between two A/Cs. This paper focuses on the performance analysis of the PAT system, exploring how the pointing error varies over time.

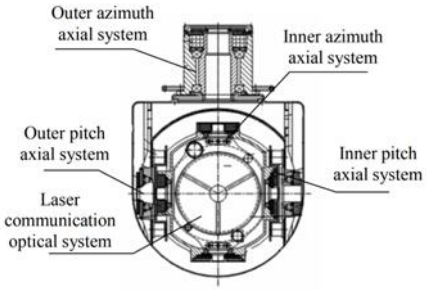


Figure 3.1 - Experimental study of the PAT system [5]

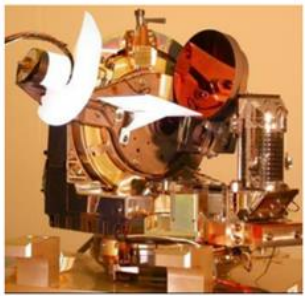

Figure 3.2 - LOLA telescope [6]

On a different level, two other papers were found to be relevant. These two are appropriate due to the information they provide, such as links and pointing budgets. The paper [7] describes a new approach to the acquisition method. Simultaneously, the paper [4] is found to be useful due to the relation between the QKD and the pointing error reports. The table below compares the performance levels of each system, providing good intuition on the performance expectations for this project.

Table 3.1 - State of the Art performances vs Lusospace requirements

| Parameter | LOLA programme [8] | Experimental Study [5] | PAT detailed design [7] | QKD [4] | Lusospace Req. |
|---|---|---|---|---|---|
| **Development level** | Tested | Tested | Tested in Lab | Designed | Test in Lab |
| **Year** | 2006 | 2018 | 2020 | 2019 | 2025 |
| **Communication** | A/C to GEO S/C | A/C to A/C | Lab | (LEO) S/C to S/C | Lab (A/C to S/C) |
| **Integration time** | 85 μs | -- | 500 μs | -- | - |
| **Acquisition time** | 10s | 18s | -- | -- | <100s |
| **Acquisition prob.** | 99% | 97% | -- | -- | >97% |
| **Acquisition dist.** | 40000km | 10 - 144 Km | -- | ~400Km | 5000 to 14500 Km |
| **Tracking accuracy** | 2.5 μrad | 8 μrad | 2 μrad | 10 μrad | 1 μrad |
| **Data rate** | 50 Mbs-1 | 2.5 $Gbs^{-1}$ | -- | -- | 1$Gbs^{-1}$ |

The papers presented above emphasize that the relevancy of the proposed goals, since there is no published work on this topic, about OC, between A/C's with MEO S/Cs.

# 4

# PAT SYSTEM ARCHITECTURE

Building upon the foundations established in the previous chapters, this section outlines the description of the chosen PAT system architecture. The design is based on the SDA protocol, [1] with the diagrams in Appendix B providing additional details to complement the general diagrams in Figure 4.1 and Figure 4.2. At the end of the chapter, specific considerations on designed architecture are presented.

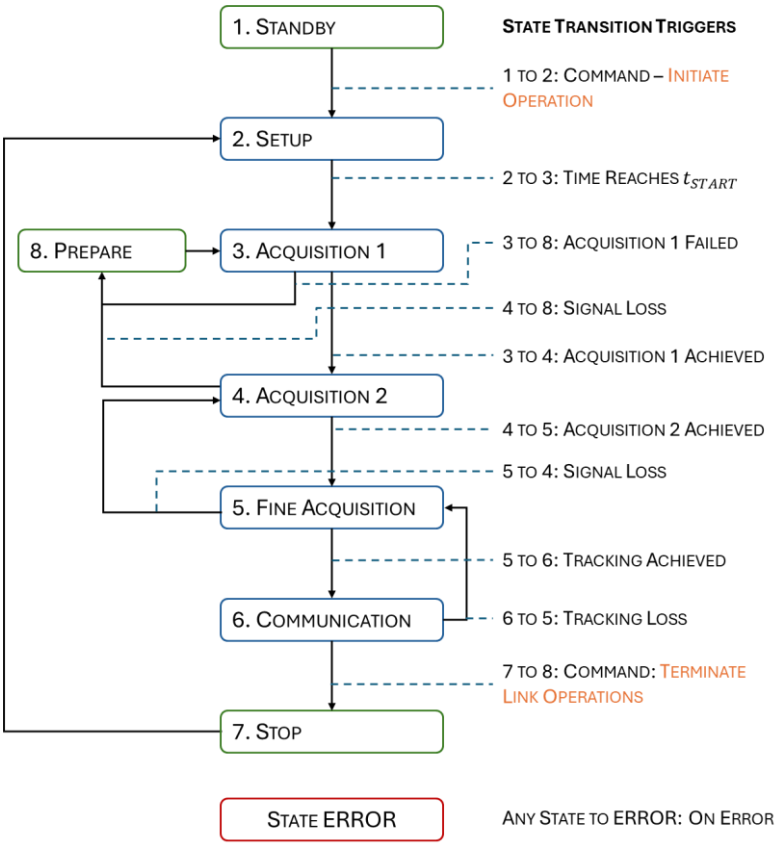


Figure 4.1 - PAT state machine based on [1]

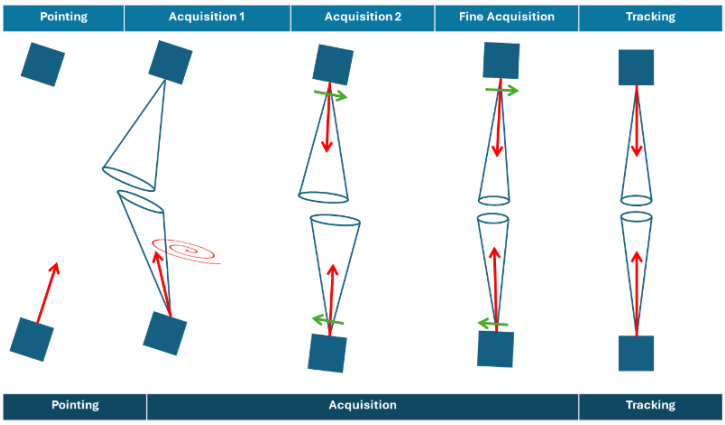


Figure 4.2 - PAT architecture representation based on [1]
Blue cone - Sensor's FOV; Red arrow - Beacon direction; Green arrow - Alignment movement

## 4.1 System-specific design considerations

This system incorporates several design features to address challenges imposed by the multiple project requirements.

One key problem concerns the CPM movement throughout the acquisition phase. Although the scan should be performed discretely due to dwell time constraints, moving the CPM in discrete steps introduces significant mechanical vibrations. Given the OH's large mass, the system would undergo large stress, making discrete movement impractical. Consequently, the CPM will move at a constant speed, avoiding large vibrations in the system.

Through this approach, the CPM continuous movement doesn't respect the dwell time required for accurate signal acquisition (unless it moves in quasistatic mode). To counter this, the FSM adjusts its position dynamically, compensating for the CPM's movement. The FSM allows the system to maintain a discrete scan by varying its angle as the CPM moves. This technique ensures that the system can still target and hold a position long enough for data acquisition.

Yet, another problem arises from the solution above. If the FSM's range is smaller than the iterative scan's step size, the mirror cannot instantaneously move between iterations. This problem leads to a dead time - a period when the system is not analysing anything because the CPM is still reaching the next scan point. The dead time parameter is fully illustrated in Figure 4.3 and given by:

$$Ang.Speed_{CPM} = \frac{Range_{FSM}(rad)}{Time_{Dwell}(s)} \quad 4.1$$

$$Time_{dead} = \frac{Angle\ between\ iterations - Range_{FSM}\ (rad)}{Ang.Speed_{CPM}\ (rads^{-1})} \quad 4.2$$

A potential solution lies in using an FSM with a more extensive range, which could reduce or eliminate this dead time. However, this trade-off comes at the cost of lower control bandwidth, which is not acceptable for the closed-loop phase.

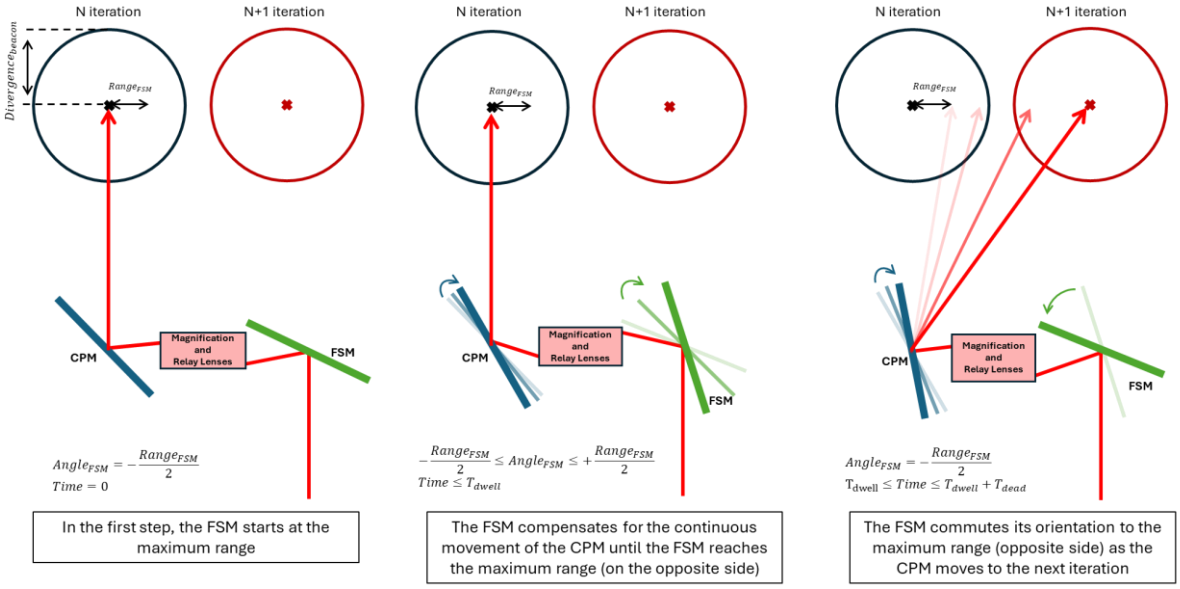


Figure 4.3 - Acquisition 1 - FSM and CPM movement representation

The CPM moves at a constant speed. The figure is not at scale. The red line illustrates how the beacon is deflected over time.

Secondly, an additional continuous movement of the CPM must be considered during both the acquisition and communication phases. This movement compensates for the relative motion between the aircraft and the satellite, ensuring that the OH continuously follows the predicted satellite's trajectory.

From the architecture perspective, the acquisition phase is split into two different stages. Initially, the system performs an open-loop acquisition (Acquisition 1). Once the ATS receives a signal from the satellite, it transitions to a closed-feedback loop phase (Acquisition 2), where each error correction is performed with the CPM. This phase is concluded once the incoming beacon is aligned within the fine pointing acquisition FOV.

# 5

# COMPONENT ANALYSIS IN PAT DESIGN

Building upon the foundations established in the PAT architecture (Chapter 4), this section introduces the chosen components for the system. This chapter focuses on the component's specifications, functions, and relevance to the overall system. In the end it is shown how the multiple components are optically connected.

A relevant factor to consider is the need for a general reference to correlate all specifications since they will feed the uncertainty budget. (Chapter 6) The exit pupil is assumed to be that reference. Consequently, all optical components lying before the telescope must scale down their specifications (by 20).

To clarify this, the telescope magnification is illustrated in Figure 5.1. The transmitting beam is represented by the right as a collimated beam. The beam goes through a lens system and a folding mirror that redirects the light to the S/C. The output beam is collimated with an increased aperture and reduced angular range. The figure below clarifies the angle factorisation since the input and output angles differ evidently. At the input, both fields are distinguishable, whereas at the output, they have a reduced angle. Finally, it is important to remember that the components involved in the beacon reflection must duplicate their specifications as the change in the angle of incidence is mirrored in the angle of reflection.

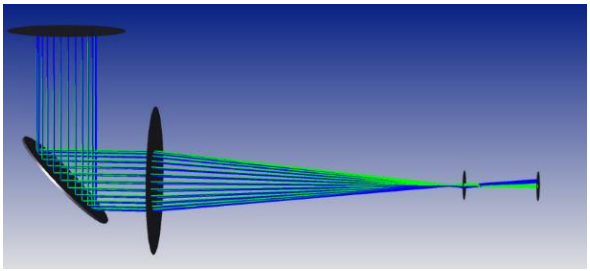

Figure 5.1 - Paraxial telescope representation (Zemax); Blue rays- 0.1 radians field, Green rays- 0 radians field

## 5.1 GNSS/INS

The GNSS/INS is responsible for measuring attitude, position, and velocity. The chosen subsystem (Figure 5.2) comprises multiple MEMS inertial sensors and two high-sensitivity GNSS receivers. Some of the sensors will measure the same dimensional parameter, such as the position measurement, resulting in a coupled estimation of its value. Advanced Kalman filtering algorithms will combine all the incoming data from these sensors to provide optimal estimations of attitude, position, and velocity.

The GNSS/INS (VN-300) also employs a technique called dynamic alignment. When this system experiences significant accelerations, the INS subsystem uses this dataset to increase the system's accuracy in specific dimensional parameters. This improved accuracy may also be referred to as increased observability.

The VN-300 uses another technique called the GNSS compass technique (Figure 2.7). Through the implementation of two antennas in the system placed at a fixed distance, (defined as baseline distance) this technique compares the carrier phase measurements of both receivers, resulting in the estimation of the aircraft's azimuth orientation (with higher accuracy).
The relevant specifications of the system are presented in Appendix C.1. Further details on the component application to our system are discussed in Chapter 6.

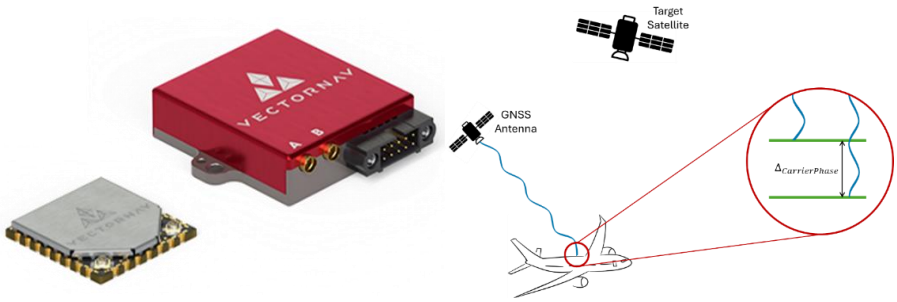


Figure 5.2 - Right - GNSS Compass technique;
Left - VectorNav VN-300 (GNSS-INS); Green Rods - GNSS Antennas; Blue Wave - Carrier Wave

## 5.2 Coarse Pointing Mechanism (CPM)

The CPM is fundamental during the acquisition process since it controls the beacon's pointing direction and performs the spiral scan. The most relevant gimbals affect the azimuth and elevation angles. The respective specifications are presented in Appendix C.2.

## 5.3 Fast Steering Mirror (FSM)

The FSM is the active correction element responsible for the optical path alignment during the fine pointing acquisition and tracking phases. The FSM must meet strict requirements, such as the frequency bandwidth and angular range. These two impositions represent a trade-off that must be considered. As referred to previously more extensive FSM range reduces the dead time (Chapter 4.1). (Chapter 7.3). However, the extended amplitude results in lower control bandwidths, limiting the error correction in the tracking phase. Appendix C.2 provides the specifications of the chosen mirror. (Figure 5.3)


Figure 5.3 - FSM - Cedrat DTT35XS-SG

## 5.4 Acquisition and Tracking Sensor (ATS)

The ATS is responsible for acquiring the S/C's signal and aligning the optical paths. It detects the misalignment between emitting and receiving beacons.

A key aspect of choosing the ATS is its integration time, which directly affects the dwell time. The integration time must be high enough to enable the signal's readability, although it cannot result in pixel saturation. To improve the sensor's readability, it is essential to minimize sun straylight and other noise sources. This can be achieved by using band-pass filters tailored to the operational spectral range. The chosen ATS (Goldeye) is displayed below. (Figure 5.4)

Throughout the acquisition and tracking processes the Goldeye exhibits a dynamic behaviour. The designed ATS HFOV matches four times the beacon divergence, ensuring the S/C's response is detectable by the OH terminal. Once the optical paths align within the Fine Pointing Acquisition (FPA) range, the ATS selects a region of interest (ROI), deactivating the outer pixels. This change increases the sensor's data readout. (Appendix C.4)


Figure 5.4 - ATS - Goldeye G-130 TEC1

## 5.5 Receiver (Rx) and emitter (Tx)

The Rx sensor is responsible for detecting the communication signal. The incoming beam is focused on an avalanche photodiode (Figure 5.5) with the described specification in Appendix C.5.

Regarding the emitter, the same laser source will feed two channels: the optical search beacon and the communication beam. An optical switch will commute the laser between the channels. For acquisition purposes, the first beacon is used instead of the second. The last one is activated once optical paths align with each communication sensor FOV. (Appendix C.6)

Figure 5.5 - High-speed response InGaAs ASM photodiode

## 5.6 System overview and other components

This subsection details how the chosen components are connected. Figure 5.6 illustrates part of the optical layout, comprising the three main optical paths.

The green divergent optical path refers to the beacon responsible for the acquisition process. Once the signal is acquired, the laser switches to the blue collimated optical path, which delivers the modulated information to the S/C. The blue trace travels towards the polarisation beam splitter (PBS), following the same direction as the green trace. The PBS transmissivity and reflectivity change according to the light polarisation. Combining orthogonal polarisations with this effect, the system directs both channels in the same trajectory.

The red path represents the incoming light, which follows a different direction from the outgoing paths. This effect is achieved with the dichroic mirror, which transmits or reflects according to the respective wavelength. Since both ATS and Rx demand the reception signal, a beam splitter is placed, ensuring that both components receive the infrared signal.

Regarding the active components, the FSM changes the direction of both the emission and reception paths. In contrast, the point-ahead mechanism only adjusts the direction of the emitting beacon. This layout ensures that only the emitting beacon is point-ahead instead of both signals.

Finally, although not present, the CPM lies after this optical layout. The traces go up through the relay and magnification lenses, leading to the CPM and then to the S/C's possible position.

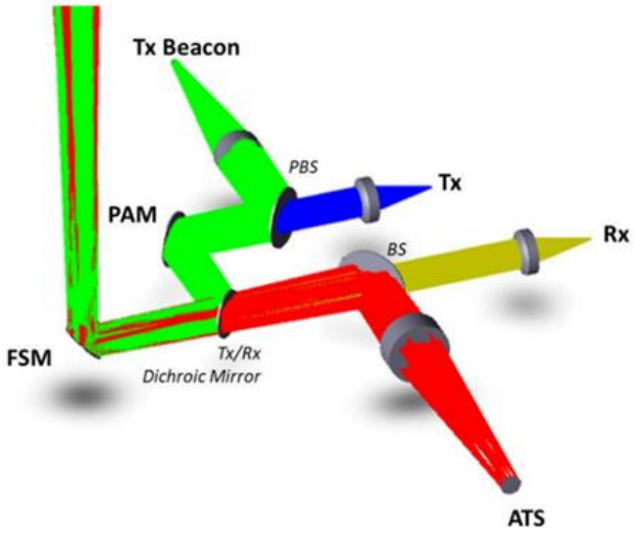


Figure 5.6 - Optical Layout;
Green - Search Beacon; Blue - Communication Beam; Red - Reception signal; PAM - Point Ahead Mechanism; BS - Beam Splitter; PBS - Polarization Beam Splitter

# 6

# PAT SYSTEM BUDGET

The concept of a budget refers to the identification and allocation of all factors that influence a specific system's performance. Careful evaluation of system budgets is critical in engineering. This chapter provides information on uncertainty and time budgets. They allow the validation of the design in later stages of the project.

The uncertainty budget is divided into two main groups: open-loop acquisition uncertainty, and closed-loop uncertainty. Appendix D.1 revisits the uncertainty theory.

## 6.1 Open-loop acquisition pointing uncertainty

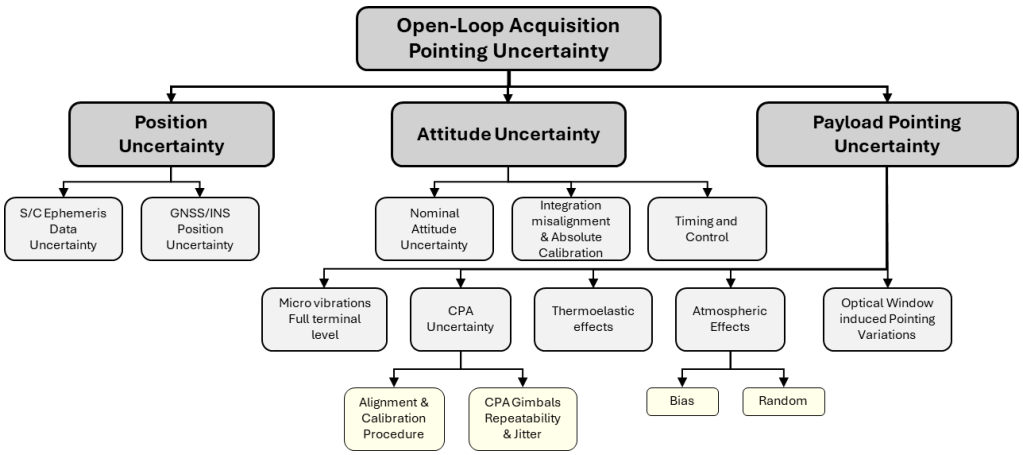


Figure 6.1 - Open-loop pointing uncertainty diagram

The respective standard deviation will be the reference for the FOU, as we referred to in the previous Chapter 2. This budget is illustrated above. (Figure 6.1) The sum of all the uncertainty contributors results in an open-loop pointing uncertainty of 5.3 milliradians. (Appendix D.5)

### 6.1.1 Position uncertainty

Position uncertainty results from the combination of ephemeris data uncertainty and OH position uncertainty. The ephemeris data is given in two line-elements set (TLE).

#### 6.1.1.1 Ephemeris uncertainty

The uncertainties inherent in the ephemeris data demand a large data set in order to be properly characterised. After analysing a paper on TLE uncertainties, an approximation of 5.5Km was allocated based on the interpretation of the q-q graphs on [9]
This uncertainty assumes the worst case, in which the satellite would be at its lowest orbit altitude (5000 km).

#### 6.1.1.2 GNSS/INS position uncertainty

The spatial uncertainty of the OH is negligible if compared to the uncertainty of the S/C position. This way, we obtain the following equation:

$$\tan(\theta) = \frac{\delta\vec{r}_{S/C}}{5000\ Km} \Leftrightarrow \theta = \arctan\left(\frac{5.5Km}{5.000Km}\right) = 1.1mrad \qquad 6.1$$

The position uncertainty budget is presented in Appendix D.3, as well as a representative illustration. (Figure  and Table )

### 6.1.2 Payload attitude uncertainty

This subsection discusses the payload attitude uncertainty based on the GNSS/INS specifications (presented in Chapter 5.1).

This measurement system will be implemented in a commercial aircraft, which means that during cruising mode, the aircraft will be under quasi-static conditions. Therefore, the dynamic alignment (Chapter 5.1) will be almost non-existent, leading to the loss of observability in the INS system and, consequently, a diminished attitude accuracy.

#### 6.1.2.1 Nominal uncertainty (random)

##### 6.1.2.1.1 Heading (azimuth)

The accuracy loss described above is mitigated by incorporating two high-sensitivity antenna receivers in the system, enabling the GNSS compass technique. The accuracy of this technique increases for greater baseline distances (between the GNSS receivers) due to higher phase

differences. The GNSS compass technique will only complement the INS when it loses accuracy in the heading parameter. (Appendix D.3)

The lowest value of heading uncertainty lies in the GNSS compass measurement (2.6 milliradians RMS for a 2-meter baseline). According to the Radome dimensions, the established baseline is expected to be feasible. Since it is anticipated that the aircraft will not lose GNSS contact, it is safe to assume the uncertainty given by this technique.

6.1.2.1.2 Pitch/Roll

The datasheet provides information for both static and dynamic situations. If the A/C ensures dynamic alignment, the uncertainty can decrease until 0.5 milliradians. In the worst-case, where the system would be fully static, the pitch/roll uncertainty can rise to 8.7 milliradians. This aircraft will likely be in an intermediate situation. During take-off, the system will have high observability on the pitch/roll measurement. Gradually, the system will lose observability in this dimensional parameter during the flight. After discussing with the supplier, the team allocated an intermediate value of 1.7 milliradians of pitch/roll nominal uncertainty.

#### 6.1.2.2 Integration misalignment (bias)

This uncertainty represents the misalignment between the A/C referential and the actual sensor referential (regarding heading, pitch, and roll). The datasheet presents a value that can be optimised through multiple calibration proceedings.

#### 6.1.2.3 Timing and control (random)

The VN-300 antenna has a finite delay time during the signal processing and information transmission (dependent on the baud rate). Combining the worst predicted delay time with the highest relative angular speed between the A/C and S/C, we obtain this uncertainty, assuming the fastest A/C orbit.

### 6.1.3 Payload pointing uncertainty

This final contribution comprises all the mechanical uncertainties, ranging from atmospheric to component contributions. The table may be observed in Appendix D.4.

#### 6.1.3.1 CPM uncertainty

The CPM will be target of alignment and calibration procedures. The strictness of these procedures, alongside the individual specifications of the gimbals, will determine the value of this contribution.

#### 6.1.3.2 Optical window deformations

The pressure difference between the OH and the atmosphere, combined with temperature variations, will result in the window deformation and, consequently, a bias pointing error of 20 microradians at 60º elevation (validated through optical and thermal analysis of the window), which is assumed to be consistent across all elevation angles.

#### 6.1.3.3 Other allocated uncertainties:

The following uncertainties result from allocations based on the team's experience due to the complexity of the characterisation of each effect.

- **Micro-vibrations** - Airplane turbulence results in random vibrations affecting pointing accuracy, especially in the open-loop acquisition phase.
- **Thermoelastic effects** - Temperature variations inside the Radome cause structural deformations. These fluctuations result in uncompensated components' misalignment.
- **Atmospheric effects** - The atmosphere between terminals introduces offset and random fluctuations in the pointing accuracy, mainly due to the turbulence around the Radome influencing the beacon's pointing direction.

## 6.2 Closed-loop pointing uncertainty

The closed-loop uncertainty encompasses the uncompensated sensing, actuation, and environmental uncertainties.

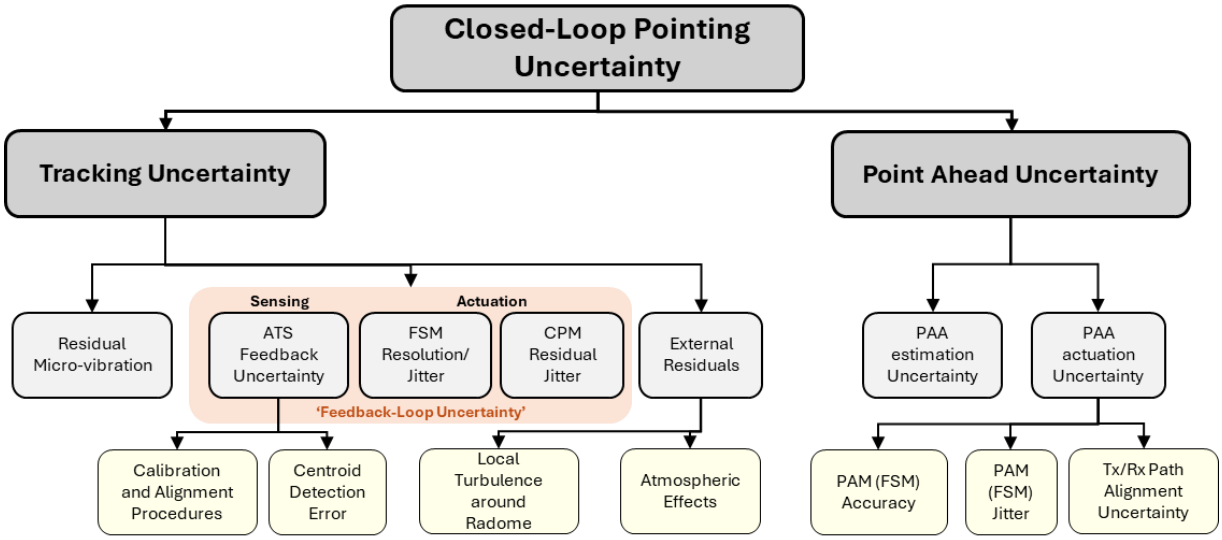


Figure 6.2 - Closed-loop pointing uncertainty

### 6.2.1 Acquisition 2 pointing uncertainty

Although acquisition 2 is already made in closed-loop mode, it doesn't accommodate high-frequency error. The uncertainties affecting this stage are given by the ATS uncertainties combined with some of the payload pointing uncertainty. (Appendix **Error! Reference source not found.**)

### 6.2.2 Tracking uncertainty

#### 6.2.2.1 Residual micro-vibrations

The FSM is used to compensate for high-frequency errors and vibrations. Naturally, the stroke range decreases for higher frequency bandwidths. Due to the complexity of analysing the vibrations in detail, the value was allocated after internal discussion.

#### 6.2.2.2 Feedback loop

##### 6.2.2.2.1 Actuation uncertainty

The actuation uncertainty arises from various factors, including FSM jitter and resolution. Additionally, we also consider some uncompensated jitter from the CPM.

##### 6.2.2.2.2 Sensing uncertainty

The sensing uncertainty comprises the centroid estimation and the alignment uncertainty. The first one varies according to the respective field, described in Chapter 6.2.4. The second is affected by the alignment errors between the Rx and the ATS central pixel, becoming an alignment requirement instead of an allocation, such as all alignment uncertainties. The total feedback-loop uncertainty is detailed in Appendix D.6.

### 6.2.3 Point Ahead Angle (PAA) uncertainty

#### 6.2.3.1 PAA estimation

Based on Chapter 2.3.2, Eq. 2.5 and the velocity uncertainties, PAA estimation uncertainty shall be given as follows:

$$\delta PAA = \frac{2}{c}\left(\delta V_{S/C} + \delta V_{A/C}\right) = \frac{2}{c}(150 + 0.05) = 1\ \mu rad \qquad 6.2$$

The A/C speed uncertainty was given by the VN-300 data sheet, opposing to the S/C speed uncertainty which was conservatively allocated based on the paper [9].

#### 6.2.3.2 Point Ahead Mechanism (PAM) actuation

Regarding the actuation mechanisms, this budget must account for the possible misalignment of the FSM, followed by its resolution and jitter. On the same perspective, the described alignment error becomes a requirement. All the PAA uncertainties are detailed in Appendix D.7.

### 6.2.4 Centroid estimation error

When the beacon enters the ATS field, its spot centroid is calculated based on its intensity distribution. However, this centroid differs from the chief ray position, which is the accurate reference for the alignment correction. This difference introduces an error that varies across the multiple optical fields, making centroid error characterisation crucial.

Zemax has a tool that allows to compute multiple spots for different fields. Since the Airy Disk is negligible compared to the spot size, it was assumed that diffraction didn't impact the centroid estimation. The centroids of the multiple field spots were calculated using NumPy, and the results are presented below. (Figure 6.3)

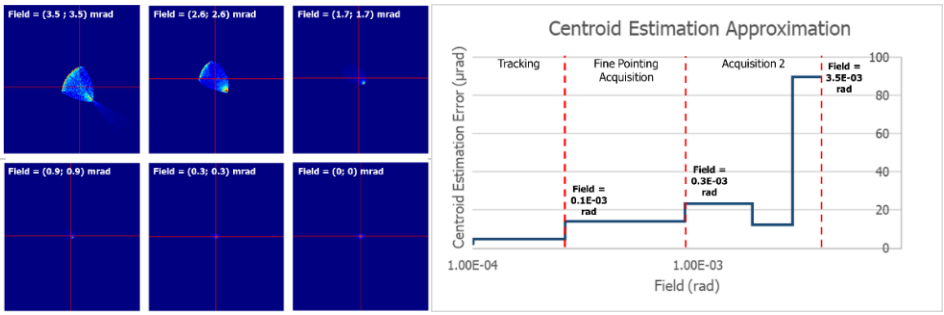


Figure 6.3 - Centroid detection analysis;
Left - Spots for each field with ATS FOV; Right - Centroid estimation Error Characterization

### 6.2.5 Time budget

The time budget plays a crucial role in determining the system's acquisition time. It has three main contributions:

1. Light takes time to travel back and forth between the A/C and the S/C. It was considered in the budget the worst case, which is a Satellite orbiting at 14500km with an angle relative to the A/C of $\pi/3$.

$$T_{light} = 2 \times \frac{14.5 \times 10^6}{3 \times 10^8 \times \cos \pi/3} \approx 192ms \qquad 6.3$$

2. Finally, the integration (or response) time of both sensors will affect the final dwell time. The integration time was allocated, based on the sensor's quantum yield, combined

with the beacon distribution along the ATS and the pixel's saturation capacity. A conservative value of 100 microseconds was allocated.

$$T_{dwell} = T_{light} + T_{S/C\ response} + T_{A/C\ response} \quad 6.4$$

3. The dead time described in Chapter 4.1 also affects the time budget depending on the chosen components. This value's allocation will vary critically according to the scan geometry. (Chapter 4.1, Eq. 4.2) This value does not directly affect the dwell time, as it does not represent the system's waiting time per iteration. Instead, the dead time reflects a system limitation that influences the overall iteration time. The iteration time, in turn, governs the total scan time, depending on the number of iterations required to complete the acquisition process.

$$T_{iteration} = T_{dwell} + T_{dead} \quad 6.5$$

## 6.3 FOV overview

After studying the PAT budget, it is possible to have a broader view of the system's behaviour. Chapter 6 allowed us to determine the beacon divergence, ATS, and tracking FOV. After computing the total open-loop pointing acquisition uncertainty, the FOU estimations (Chapter 2.2.1) are possible. Allocating 2.5σ results in a theoretical acquisition probability of 99%.

Finally, the Fine Pointing Acquisition (FPA) FOV will be given by 90% of the FSM deflection range (ensuring a high frame rate). However, this FOV has a margin. The system will only transition to the next phase if the beacon spot is within a tolerance window. This window prevents the system from continuously commuting between acquisition 2 and fine pointing acquisition. Figure 6.4 quantises and illustrates the discussed FOVs.

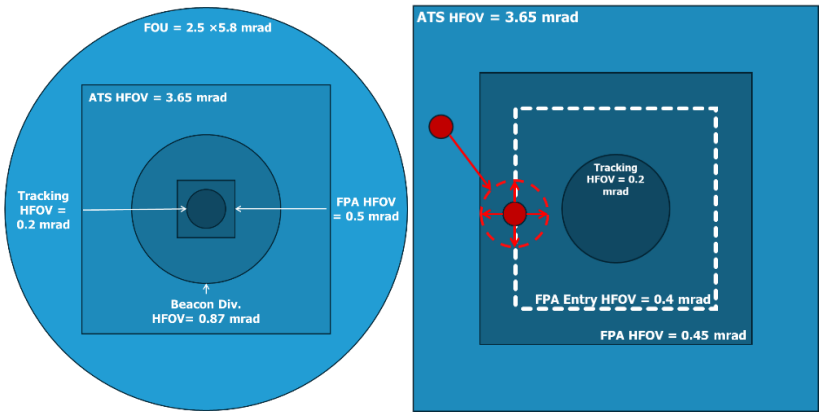


Figure 6.4 - HFOV (exit pupil)

This caption illustrates every FOV involved in the PAT system configuration.

# 7

# UNCERTAINTY ANALYSIS AND MODELLING

One of the main goals of this thesis is to assess the system's compliance with the given requirements. An emulator was designed and programmed from scratch in Python to perform this validation. This chapter outlines the building blocks of this numerical analysis, which comprises three main categories.

Firstly, the open-loop acquisition is deeply covered, starting from the scan's definition and parameterization to the acquisition and geometry analysis of the respective scan. Second, the CPM movement is described mathematically, addressing the multiple starting positions of the estimated satellite position and the resultant drift from the relative motion between both bodies. Finally, the structure of closed-loop phase simulation is explained.

It is important to note that most of the images represented, do not reflect the real scan parameters. The values have been exaggerated to facilitate the understanding process of the different concepts.

## 7.1 Open-loop acquisition

The acquisition phase was simulated to analyse parameters such as the average acquisition time and the S/C's acquisition probability. (Chapter 7.1.5)

The program generates a random position, according to the S/C Gaussian distribution. Then, the Python code performs multiple iterations starting from the centre of the spiral. The user defines the shape of the spiral and the cartesian distance between the iterations. (Chapter 7.1.2) Once the S/C is within one of the iteration effective radii, the elapsed time is recorded, and it is counted as one successful acquisition. Figure 6.4 presents an example of one acquisition process over time. The black circles are deviated from the red spiral due to the CPA pointing uncertainty.

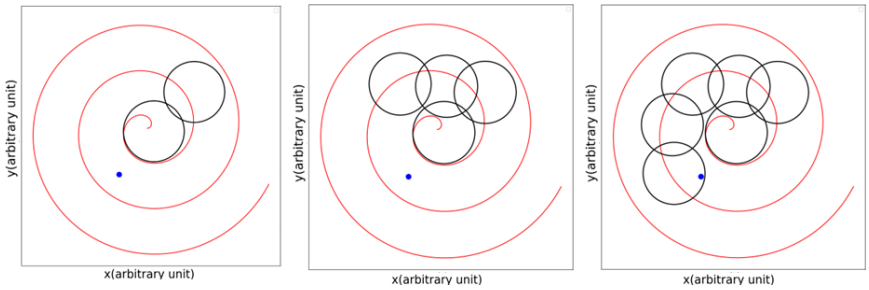


Figure 7.1 - Acquisition representation over time- XY
Red spiral - Ideal scan trace; Blue dot - Satellite position; Black circles - Scan iterations

At the same time, the emulator characterises the not-identified and overlapped areas in the open-loop acquisition phase.

### 7.1.1 Spiral definition

In practice, the scan is represented as three-dimensional vectors that start in the OH and propagate to infinity, like the search beacon. All the two-dimensional figures presented below represent the upper view of these normalized vectors.

In fundamental terms, the spiral to be performed is not an Archimedean spiral. However, its upper view can be reasonably approximated as one, due to the small angles of the spiral. Appendix E.4 provides a detailed explanation of this approximation.

$$\begin{cases} x = r \times \cos\theta \ \ (m) \\ y = r \times \sin\theta \ \ (m) \end{cases} \qquad r \in [0, \tan FOU \approx FOU] \qquad \theta = \frac{2\pi}{Distance_{between\ turns}} \times r \tag{7.1}$$

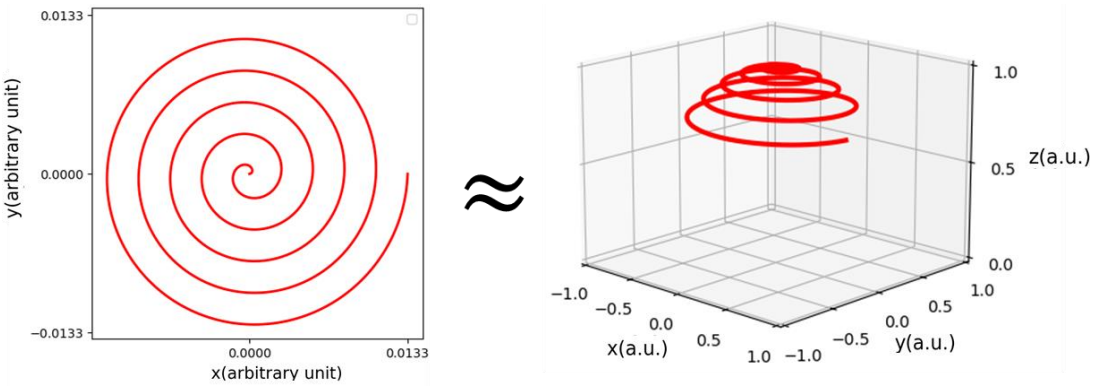


Figure 7.2 - Spiral approximation.

### 7.1.2 Scan parameters

This subsection presents the fundamental parameters that will determine the overall performance of the acquisition scan.

#### 7.1.2.1 Iterative Step

As expressed in Chapter 4.1, the scan must be discrete. Therefore, it is necessary to define an iterative step. In this case, it will be given as a cartesian distance between consecutive circles (or iterations). Figure 27 displays a representation of the iterative step.

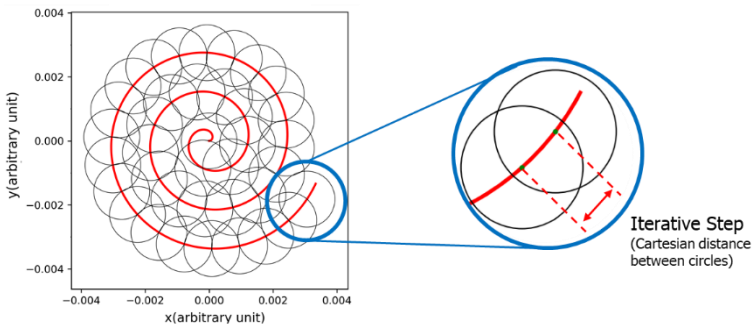


Figure 7.3 - Iterative step representation

#### 7.1.2.2 Spiral Step

The spiral step parameter represents the distance between each turn. As was already explicit in Chapter 2.2.3, the spiral step ($L_\theta$) affects the scan's radial overlap, as well as the acquisition time and probability, (Chapter 7.1.5).

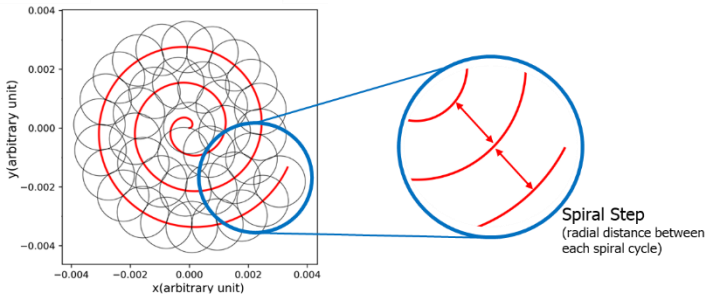


Figure 7.4 - Spiral step representation

#### 7.1.2.3 Field Of Uncertainty (FOU)

The FOU, already described in Chapter 2.2.1, is now represented as a specific parameter of the simulation.

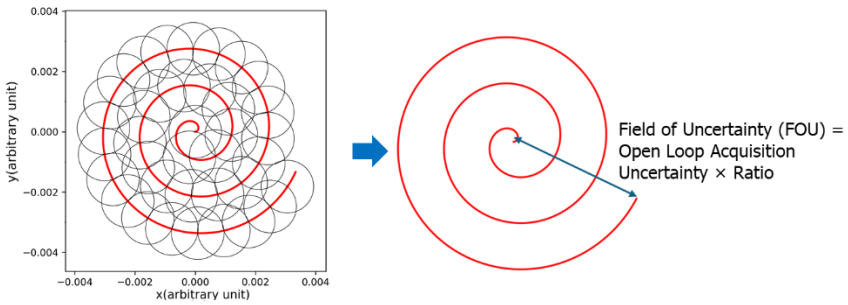


Figure 7.5 - Field of Uncertainty representation

### 7.1.3 CPM pointing uncertainty (random)

The scan simulation must account for multiple uncertainties, such as the random components of the CPM pointing uncertainty. The circle's position shall be shifted for each iteration based on this uncertainty.

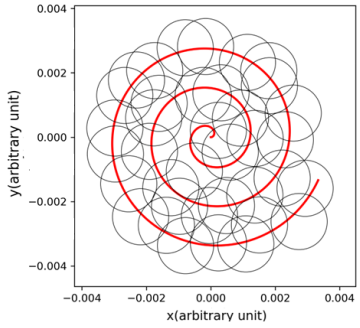


Figure 7.6 - Scan representation with payload pointing uncertainty

### 7.1.4 Satellite's position distribution

Since the satellite's position follows a normal distribution, we perform multiple trials to build a trustworthy statistic. Note that the satellite's distribution will follow the random standard deviation of the open-loop acquisition uncertainty. The bias uncertainty will reflect on a shift of the S/Cs' position relative to the centre of the spiral scan. (Chapter 6.1)

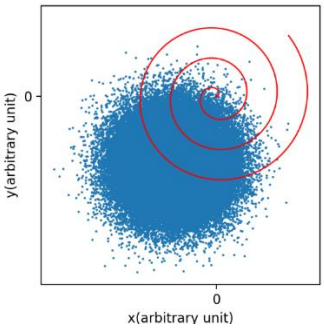


Figure 7.7 - Satellites distribution relative to the spiral scan

### 7.1.5 Acquisition 1

To analyse the predicted mean acquisition probability, the successful acquisitions are counted. The following computation reflects the respective acquisition probability.

$$P_{Acquisition}\ (\%) = \frac{Successful\ Trials}{Total\ Trials} \times 100 \qquad 7.2$$

Simultaneously, for each successful trial, the acquisition time is recorded. In the end, the arithmetic average and standard deviation values are calculated.

$$\overline{T_{Acquisition}}\ (s) = \frac{\sum_i^{Total\ Trials} T_{i\ acquisition}}{Total\ Trials} \qquad 7.3$$

The descriptive diagram of this simulation lies in Appendix E.2, Figure . The respective diagram details each uncertainty contribution input

### 7.1.6 Spiral geometry

This subsection explores the overlapped area of the scan, as well as the not-identified area of the same scan, through the Montecarlo method. The emulator generates samples from a uniform distribution, which will fit inside a square with a length given by:

$$Lenght_{Square} = FOU + Random\ Uncertainty_{CPM} \qquad 7.4$$

This way, independently of the random position of the spiral's circles, they will always fit inside this square. after the random generation, the encircled points are properly counted. The overlapped area is computed as follows:

$$Numeric\ Overlap(\%) = \frac{Counted\ Samples}{Total\ Samples} \times \frac{A_{square}}{N_{circles} \times A_{Circle}} \qquad 7.5$$

Some accurate algebraic methods exist. However, they are too demanding for the computer. Simultaneously, these Montecarlo data allowed to compute the percentage of not-identified area within an effective radius. The effective radius was obtained empirically. (0.93×FOU) After counting the encircled points, the not-identified area is computed as follows:

$$Not\ identified\ area\ (\%) = \frac{Not\ identified\ points}{Total\ Points\ within\ the\ effective\ radius} \times 100 \qquad 7.6$$

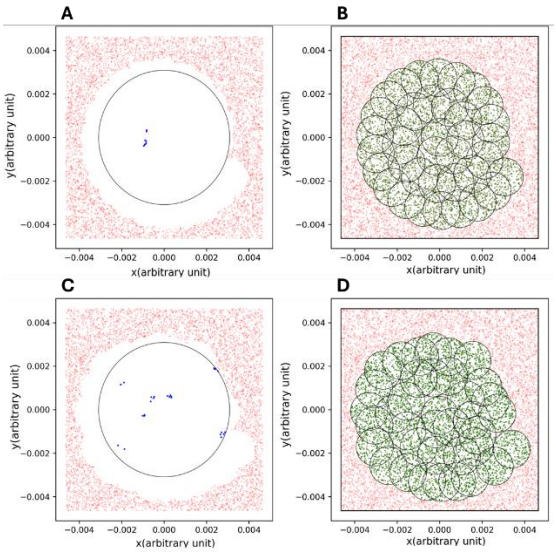


Figure 7.8 - Numeric analysis representation

A and B - Simulation without uncertainties; C and D - Simulation with uncertainties

Left - Not identified area within scan (blue dots); Right - Identified area (green dots); Red dots - Unidentified area

## 7.2 CPM movement characterization

The main goal at this stage lies in describing the gimbals' movement (in spherical coordinates) throughout the acquisition process. To achieve that, it is mandatory to consider the movement of the satellite relative to the A/C terminal. This demands the use of Euler transformations and one other transformation, described below. Appendix E.5 exhibits a deeper understanding of these rotation matrices alongside the coordinate's conversion from the earth centre to the A/C's reference frame. (Appendix E.3)

### 7.2.1 Euler transformation

The Euler transformation allows the rotation of the reference frame around the 3 orthogonal axes. In this case, the spiral shall rotate along the z-axis and then the y-axis. This combination of rotations is performed in an intrinsic way, which means that the rotation is always performed relative to the recently rotated reference frame. Applying this matrix will accurately describe the movement of the gimbals (along the spiral scan) for any combination of initial angles.

### 7.2.2 Matrix rotation along an arbitrary axis

This rotation aims to represent the satellite's drift over time. It will allow the spiral to rotate progressively relative to the A/C's terminal in any possible direction throughout the scan process.

$$Absolute\ Scan\ coordinates\ (x, y, z) = R_{Euler} \times R_{Arbitrary\ Axis} \times Scan\ Point \qquad 7.7$$

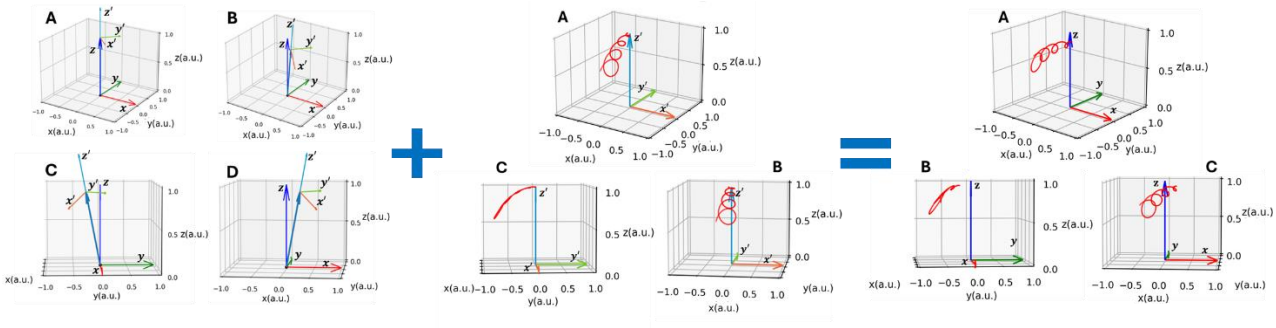


Figure 7.9 - Rotation matrices combination. Detailed in Appendix E.4 [The combination of the initial frame rotation with the drift rotation matrix around an arbitrary axis results in an accurate representation of the gimbals' movement throughout the acquisition process (Python)
Azimuth rotation $= -\frac{\pi}{4}$; Elevation rotation $= \frac{\pi}{8}$ ; Drifting angle $= -\frac{\pi}{2}$]

## 7.3 Closed-loop phase

The closed-loop phase encompasses the simulation on acquisition 2, fine pointing acquisition and tracking phases since they are similar regarding the closed-loop method. Each sub-phase addresses a specific pixel window and to its respective pointing uncertainty. (Figure 7.10) The first two phases are analysed by calculating the average number of iterations required to transition the system to the next phase. Throughout the tracking phase, the emulator evaluates how the estimated errors affect the tracking stability. The representative diagram of this emulator lies in Appendix E.5.

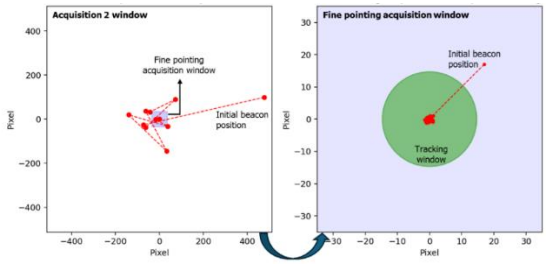


Figure 7.10 - Closed-loop phase representation (the system transitions from left to right, as Chapter 4, refers) Left - Acquisition 2; Right - Fine pointing acquisition and tracking; Blue Square - Representative fine pointing acquisition window; Green Circle - Correspondent FOV of the Rx sensor; Red Dots - Spot's centroid evolution throughout the alignment process

# 8

# PERFORMANCE

## 8.1 Open-loop phase

Based on the groundwork laid in the previous chapter, this section assesses how well the system meets the specified requirements and provides the parameters window that ensures compliance with them. The system is evaluated under its most challenging conditions, which occur when the spacecraft is at its highest altitude and at the maximum angle allowed by the OH. One of the analyses conducted is depicted in Figure 8.1. It is important to remember that both spiral and iterative steps are inputted as a ratio relative to the beacon's divergence.

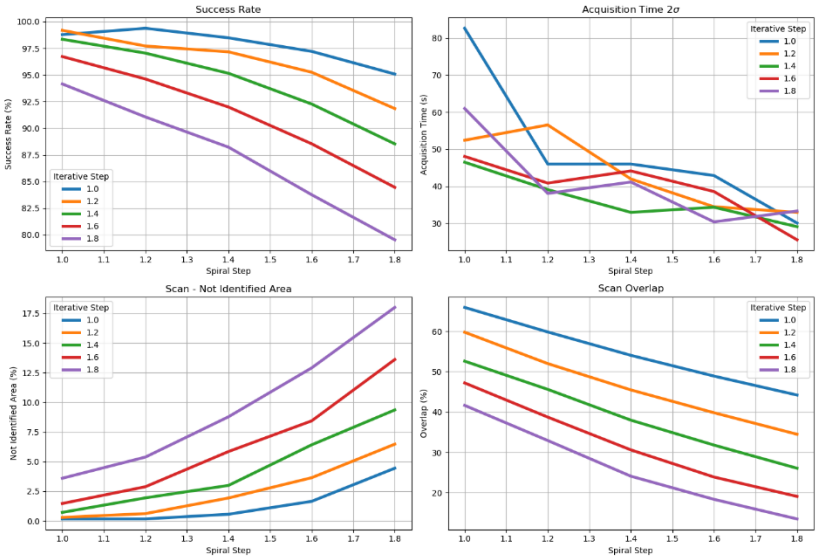


Figure 8.1 - Acquisition analysis (2.4 sigma - $10^7$ trials per parameter configuration)
The acquisition time plot has a 97.7% confidence interval.

The graphs' observation allows to assess that, in general, increasing the spiral and iterative steps, (Chapter 7.1.2) reduces the success rate, acquisition time, and overlap. Simultaneously, increasing the input parameters results in a larger not-identified area. These trends are consistent with expectations. As the step size increases, there is a higher chance of leaving gaps between the iterations, which speeds up the scanning process but may also lead to a lower success rate.

Although the general trends appear consistent, there are some unintuitive results, mainly observed in the acquisition time plot. Further investigation must consider these fluctuations. Given the high acquisition time variability, it is fundamental to have a conservative approach to the optimal parameters' selection. Parameters that result in longer acquisition times, despite offering higher success probabilities, should be avoided to ensure the system's compliance. The optimal window falls within the following ranges:

- Relative angular step: 1.2–1.4,
- Relative spiral step: 1.0–1.4,
- Sigma ratio: 2.4–2.6

The table below shows a more in-depth evaluation of a specific set of parameters. The CPM movement progression, for the conditions outlined in this table, is depicted in Figure 8.2. The acquisition probability standard deviation is computed based on the 10 trials of $10^8$ cycles

Table 8.1 - Optimal configuration example

| Iterative step | Spiral step | FOU $(\sigma \times ratio)$ | Acquisition probability | Acquisition time $\overline{T} \pm \sigma$ | Cycles |
|---|---|---|---|---|---|
| 1.1mrad | 1.1mrad | 5.3mrad×2.5 | ~99±0.3 % | ~13±13 seconds | $10\times10^8$ |

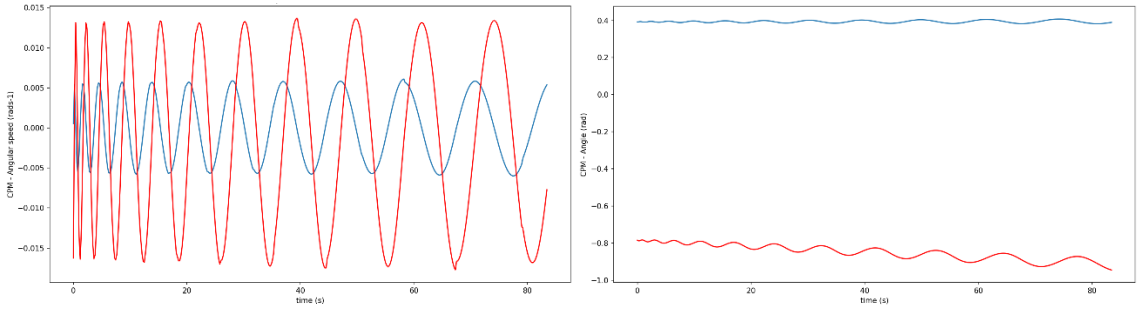


Figure 8.2 - CPM movement; Left - Angular speed; Right - CPM angle; [Red - Azimuth; Blue - Elevation; Azimuth rotation $= -\frac{\pi}{4} rad$; Elevation rotation $= \frac{\pi}{8} rad$; Drifting angle $= -\frac{\pi}{2} rad$ ; Drift rate = $0.5 mrad$]

## 8.2 Closed-loop phase performance

The closed-loop analysis ends up being much simpler to simulate. since there are fewer random variables in place. The selected FOV resulted, we obtained the following results:

Table 8.2 - Closed-loop performance

| Closed-Loop sub-phase | Pixel Window | Uncertainty Contributors | Average Convergence Iterations | Std. Convergence Iterations | Convergence Cycles |
|---|---|---|---|---|---|
| Acquisition 2 | 1024 | 230 urad | 4 | 3 | $10^3$ |
| Fine Pointing Acquisition (FPA) | 40 | | 1 | 1 | |

The tracking phase showed a tracking accuracy of 4.2 microradians. Assuming the CPA iteration frequency to be 10Hz, both phases would require approximately two seconds.

### 8.2.1 Centroid estimation time

It is fundamental that the centroid estimation is performed as fast as possible since it will feed the system in real time. To optimize the computation time, the emulator used the package Numba, which compiles functions to the machine level. This way, the emulator outputs performances similar to those of lower-level languages but using Python. The first time the function runs, it takes additional time to compile the Python code. However, after that compilation, the centroid estimation takes a maximum of 0.3 milliseconds (performed in Intel Core I5). This time can be further improved through the removal of null matrix elements, before the centroid computation.

This time establishes a maximum correction frequency of approximately 3kHz, which complies with the FSM correction frequency.

## 8.3 Requirements compliance

The table below (Table 8.3) compares the requirements with the system's performance. While some specifications are compliant, the open-loop pointing uncertainty falls short due to inherent limitations within the system. In the tracking phase, the accuracy does not meet the required standards. Since this requirement is critical, efforts will be focused on improving accuracy through ATS calibration for more precise centroid estimations. Laboratory tests showed that this uncertainty could be reduced to 0.1 pixels. (0.7 μrad). Additionally, the FSM control

bandwidth is lower than required, as increasing the frequency would bring it closer to resonance, which would increase the pointing error.

Given these issues, it is crucial to further study the closed loop phase's performance since it is highly dependent on multiple uncharacterized factors, such as the dynamic error and the uncompensated vibrations during the tracking phase. (Chapter 6.2)

Table 8.3 - Requirements Analysis

| Critical parameters | Open-loop pointing acquisition uncertainty | Acquisition time | Acquisition probability | Tracking accuracy | Tracking bandwidth |
|---|---|---|---|---|---|
| Requirement | 5.1 mrad | <100 s | >97% | 1.0 μrad | 1kHz |
| Performed | 5.3 mrad | <39 s ($2\sigma$) | ~99% | 4.2 μrad | 900Hz |

.

# 9

# Conclusion

This thesis comprised the design and validation of a PAT system. This system was found to comply with some of the requirements. However, there is more work to be done. Practically speaking, the project will move to the assembly integration and testing phase, where every conceptual approach will be tested and experimentally validated.

On a more conceptual level, further study is needed to better characterize the vibrations affecting the system. Additionally, a deeper exploration of the FSM's behaviour at higher frequencies is required to optimize its correction capabilities. Regarding open-loop acquisition, investigating the non-linearities in the scanning process and examining the potential benefits of using a variable iterative step would be worthwhile areas for future work.

The greatest challenges encountered during this thesis involved translating specific project needs into a structured design approach with the necessary approximations and simplifications. These challenges pushed my engineering process to new limits, forcing me to think more critically and creatively. Above all, it was rewarding to see the convergence of various technical areas towards a common goal within the scope of a smaller project, which itself contributes to the broader objectives of larger entities, such as ESA.

# BIBLIOGRAPHY


[1] D. M. Tournear, "Optical Communications Terminal (OCT) Standard Version 3.0.1," 2023.

[2] B. Mukherjee, "Optical Networks Series editor." [Online]. Available: http://www.springer.com/series/6976

[3] H. Hemmati, "Near-Earth Laser Communications; Second Edition." [Online]. Available: https://www.crcpress.com/Optical-

[4] D. Naughton, R. Bedington, S. Barraclough, T. Islam, D. Griffin, and B. Smith, "Design considerations for an optical link supporting intersatellite quantum key distribution," *Optical Engineering*, vol. 58, no. 01, p. 1, Jan. 2019, doi: 10.1117/1.oe.58.1.016106.

[5] Y. Lei, X. Li, and L. Zhang, "Experimental Study on PAT System for Long-Distance Laser Communications Between Fixed-Wing Aircrafts," *Photonic Sensors*, vol. 9, no. 2, pp. 170–178, Jun. 2019, doi: 10.1007/s13320-018-0522-9.

[6] V. Cazaubiel *et al.*, "LOLA: a 40.000 km optical link between an aircraft and a geostationary satellite," SPIE-Intl Soc Optical Eng, Nov. 2017, p. 129. doi: 10.1117/12.2308161.

[7] M. Zhang, B. Li, and S. Tong, "A New Composite Spiral Scanning Approach for Beaconless Spatial Acquisition and Experimental Investigation of Robust Tracking Control for Laser Communication System with Disturbance," *IEEE Photonics J*, vol. 12, no. 6, Dec. 2020, doi: 10.1109/JPHOT.2020.3031260.

[8] V. Chorvalli, L. Le Hors, L. Vaillon, and G. Planche, "Optical communications between an aircraft and a geo relay satellite: design and flight results of the LOLA demonstrator," SPIE-Intl Soc Optical Eng, Nov. 2017, p. 10. doi: 10.1117/12.2308195.

[9] D. Racelis and M. Joerger, "High-Integrity TLE Error Models for MEO and GEO Satellites."

[10] W. Tan, T. C. Jen, and M. Gao, "Medium earth orbit and inclined geosynchronous orbit satellite control strategies optimization based on the function approximation method,"

in *Proceedings of the Institution of Mechanical Engineers, Part G: Journal of Aerospace Engineering*, Jun. 2009, pp. 475–484. doi: 10.1243/09544100JAERO412.

# A

# THEORETICAL BACKGROUND

## A.1 Point Ahead Angle

This Appendix subsection presents a simple derivation of the point ahead angle. Assuming the small angle approximation, we may consider the S/C movement as the body number one with constant speed and altitude. The light (body number two) is emitted with an angle $\frac{\alpha}{2}$ relative to the vertical. Both bodies started at the same x position. (Figure )

$$\begin{cases} x_1 = v_{relative} \times t \\ y_1 = d \end{cases} \quad \begin{cases} x_2 = c \times t \times \sin\frac{\alpha}{2} \\ y_2 = c \times t \times \cos\frac{\alpha}{2} \end{cases} \quad \Rightarrow \quad y_2 = y_1 \Leftrightarrow t = \frac{d}{c \times \cos\frac{\alpha}{2}}$$

$$x_2 = x_1 \Leftrightarrow v_{relative} \times t = c \times \sin\frac{\alpha}{2} \times t \Leftrightarrow \frac{v_{relative}}{c} = \sin\frac{\alpha}{2} \approx \frac{\alpha}{2} \Leftrightarrow \alpha = \frac{2v_{relative}}{c}; \quad \text{A.1}$$

$$\alpha \approx \text{small angle}$$

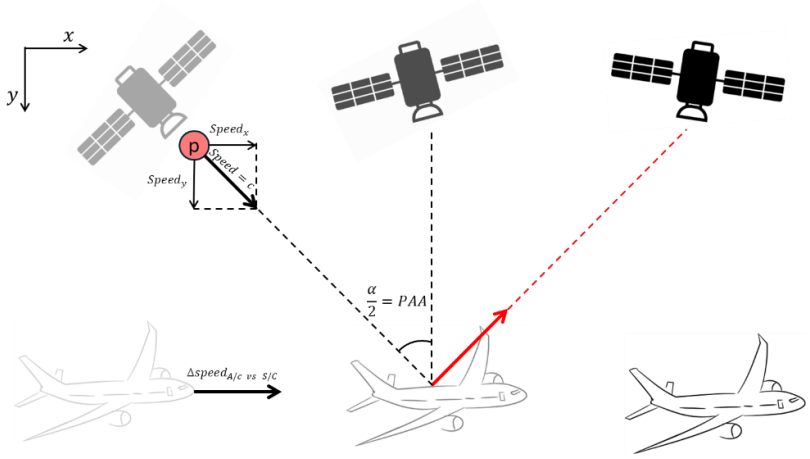


Figure A.1 - Point Ahead Angle represented

"p" - Infra-red Photon

# B

# PAT SYSTEM ARCHITECTURE

## B.1 Architecture description

| ID | Name | Description | Entry Criteria | Exit Criteria |
|---|---|---|---|---|
| 1 | **Standby** | OCT waits for further commanding. | | Command Received: Initiate Link Operation → Setup |
| 2 | **Setup** | After a new link command is received, the OCT is configured according to the link parameters and the coarse pointer starts to move towards the target trajectory | Command Received: Initiate Link Operation Required Parameters: See Table 2-2 | OCT has slewed into position and terminal has been configured ahead of $t_{start}$ being reached Starting time $t_{start}$ is reached →Acquisition Phase 1 |
| 3 | **Acquisition Phase 1** | During acquisition phase 1 the lead OCT scans the given cone of uncertainty. | | Configuration Parameter Phase 1 duration reached ($\delta_{Acq1}$) →Acquisition Phase 2 |
| 4 | **Acquisition Phase 2** | During acquisition phase 2 the lead OCT transmit and receive at the same time. This terminal operates in a feedback loop making use of a Wide FoV detector to measure the misalignment between Optical Paths. | | Uncertainty reduced such, that target is within FOV of the fine acquisition area of the ATS →Fine Acquisition<br><br>Timeout waiting for further hits → Prepare |
| 5 | **Fine Acquisition** | During fine acquisition, the lead OCT deactivates the outer pixels of the detector and performs the fine acquisition in a feedback loop (with higher bandwidth). | | Stable tracking established, continuous receive signal → Communication.<br><br>Timeout waiting to establish tracking → Prepare |
| 6 | **Communication** | Bidirectional data link is established. The laser channel commutes to the collimated beam | | Command Received: $\delta_{LmtGoStop}$ → Stop<br><br>Tracking signal lost → Fine Acquisition |
| 7 | **Stop** | The link is terminated by command or due to a failure condition. The OCT goes back to standby | | Laser and all mechanism stopped and goes back to standby |
| 8 | **Prepare** | Prepare to reestablish the Link | | OCT has slewed into position based on latest ephemeris prediction and terminal configuration and then $t_{start}$ is reached |

Figure B.1 - PAT state machine description based on [1]

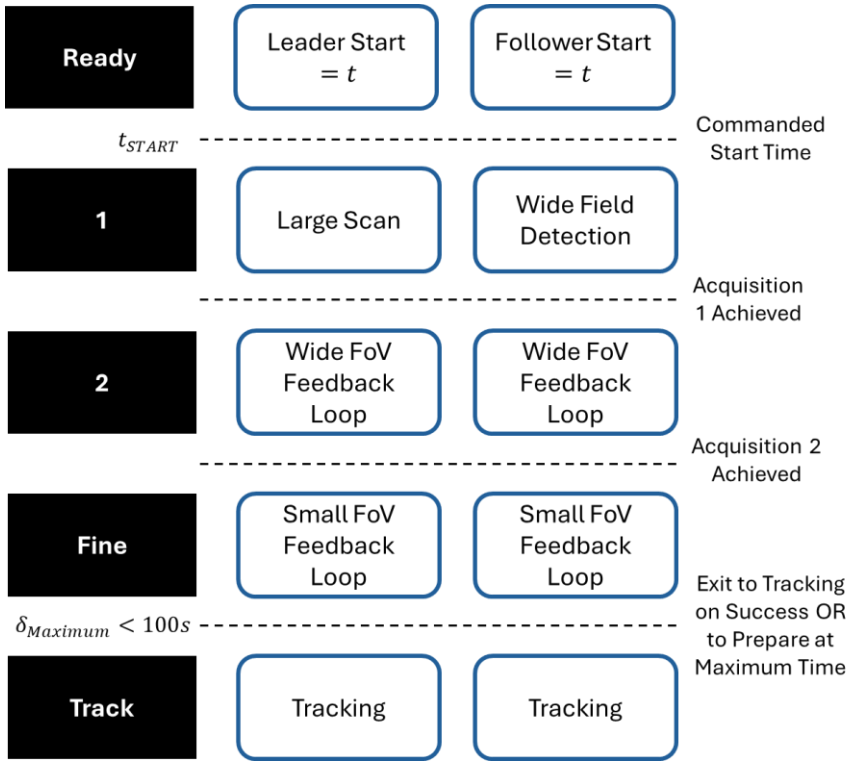


Figure B.2 - PAT system architecture described

# C

# COMPONENT SPECIFICATIONS TABLES

## C.1 GNSS/INS

Table C.1 - GNSS/INS specifications

| Parameter | Specification | Unit | Remarks |
|---|---|---|---|
| **Attitude specifications** | | | |
| **Range (Heading, Roll)** | ±π | rad | |
| **Angular resolution** | 17.5 | μrad | |
| **Range (Pitch)** | ±π/2 | rad | |
| **Heading accuracy (INS)** | 3.5 | mrad, 1σ | Assuming enough accelerations for dynamic alignment |
| **Heading accuracy (GNSS-compass)** | 5.2 to 10.5 (0.5m Baseline) | mrad, RMS | Depending on Satellite Based Augmentation System (SBAS), clear view of the sky, good multipath environment, compatible GNSS antenna, and measurement duration period. |
| | 2.6 to 5.2 (1.0m Baseline) | | |
| | 1.4 to 2.6 (2.0m Baseline) | | |
| **Pitch/Roll accuracy (static)** | 8.7 | mrad, RMS | |
| **Pitch/Roll accuracy (INS)** | 0.5 | mrad, 1σ | Assuming enough accelerations for dynamic alignment |

| | | | |
|---|---|---|---|
| **Heading mounting misalignment** | 2.6 | mrad, 1σ | |
| **Pitch/Roll mounting misalignment** | 1.7 | mrad, 1σ | |
| **Position Specifications** | | | |
| **Horizontal position uncertainty** | 1.0 | m, RMS | Same remark as Heading Accuracy |
| **Vertical position uncertainty** | 1.5 | m, RMS | |
| **Velocity accuracy** | <0.05 | $ms^{-1}$ | |

## C.2 Coarse Pointing Mechanism (CPM)

Table C.2 - Aerotech Gimbals Specifications

| Parameter | Azimuth | Elevation |
|---|---|---|
| Model | ALAR100LP | APR200DR-155 |
| Range | 2π rad | -87mrad to+0.4π rad |
| Resolution | 0.1 μrad | 0.3 μrad |
| Accuracy | ±9.7 μrad | ±15 μrad |
| Repeatability | ±2.4 μrad | ±5 μrad |
| Wobble | ±19.4 μrad | ±10 μrad |
| Max Velocity | $1.7\pi$ $rads^{-1}$ | $20\pi$ $rads^{-1}$ |
| Jitter | ±1 μrad | ±1 μrad |

## C.3 Fast Steering Mirror (FSM)

Table C.3 - Fast Steering Mirror specifications

| Parameter | Specification (exit pupil) | Unit |
|---|---|---|
| FSM range (exit pupil) | ±0.125 | mrad, 1σ |
| Angular resolution (exit pupil) | 0.05 | μrad |
| Control bandwidth (-3dB) | >600 | Hz |
| Maximum mirror diameter | 15 | mm |

## C.4 Acquisition and Tracking sensor (ATS)

Table C.4 - Acquisition and Tracking sensor specifications

| Parameter | Specification | Unit |
|---|---|---|
| Resolution | 1280(H) × 1024(V) | px |
| Spectral range | 400 - 1700 | nm |
| Pixel size | 5 | µm |
| Max. frame rate $_{\text{Full Resolution}}$ | 93 | fps |
| Max. frame rate $_{36\times36\text{px}}$ | >1000 | fps |
| Max. FOV (exit pupil) | ±3.5 | mrad |

## C.5 Receiver sensor (Rx)

Table C.5 - Receiver sensor specifications

| Parameter | Specification | Unit |
|---|---|---|
| Diameter | 0.080 | mm |
| FOV (exit pupil) | ±0.2 | mrad |
| Data Readout rate | 1 | GHz |

## C.6 Laser emitter (Tx)

Table C.6 - Laser emitter specifications

| Parameter | Specification | Unit |
|---|---|---|
| Divergence acquisition beacon | ±0.873 | mrad |
| Divergence communication beam | (diffraction limit) $\pm6.1\times10^{-3}$ | mrad |

# D

# UNCERTAINTY TABLES

## D.1 Uncertainty revisited

The uncertainties split themselves in 2 main groups.

**Bias uncertainty**

The Bias uncertainty represents a fixed offset that cannot be compensated by the system. Usually, these uncertainties arise from the misalignments, calibrations performed, thermal deformations, and so on. Consequentially all these bias (also referred as class "F") uncertainties are summed up linearly as the equation below shows:

$$\delta_{Total\ Bias} = \sum_{i_{bias}}^{n} \delta_{i_{bias}} \qquad \text{D.1}$$

**Random uncertainty**

The Random uncertainty, (referred as class R) comprises all the uncertainties that will follow a Gaussian distribution with a specific standard deviation. These uncertainties will be all summed up as:

$$\delta_{Total\ Random} = \sqrt{\sum_{i_{random}}^{n} \left(\delta_{i_{random}}\right)^2} \qquad \text{D.2}$$

**Total uncertainty**

In the end, the total uncertainty will be given by:

$$\delta_{TOTAL} = \delta_{Total\ Random} + \delta_{Total\ Bias} \qquad \text{D.3}$$

## D.2 Position uncertainty

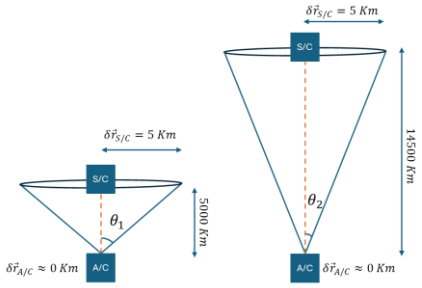


Figure D.1 - Position uncertainty representation

The uncertainty in the ephemeris data is derived from the paper mentioned above. [9] The graphs provided below depict a comparison between the error distribution of the satellites in medium Earth orbit (MEO) and a Gaussian distribution. The study discovered a strong correlation between both distributions and calculated the average ephemeris data error as well as its standard deviation. The slope of the line represents the sample standard deviation, while the y-intercept represents the sample mean. This portion of the paper approximates the distribution within 3 $\sigma$ (99.9% confidence). The graphs in Figure pertain to all uncertainty orthogonal directions: radial, along-track, and cross-track.

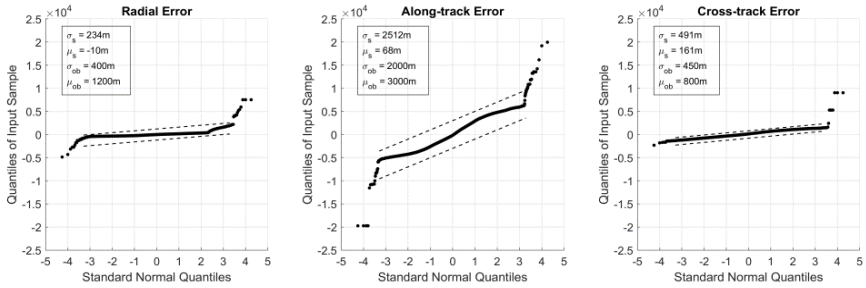


Figure D.2 - TLE errors [9]

The table below (Table ) confirms the allocated uncertainty, based on the over-boundary estimations, totalizing a 5.5km value.

Table D.1 - TLE errors [9]

| TLE errors | $\sigma_{ob}$ | $\pm\mu_{ob}$ |
|---|---|---|
| Radial error (m) | 400 | 1200 |
| Along-track error (m) | 2000 | 3000 |
| Cross-track error (m) | 450 | 800 |
| **Total error (m)** | **2089 (RSS)** | **3329 (Sum)** |

Table D.2 - Position Uncertainty

| Uncertainty contributor | Value | Unit | Type |
|---|---|---|---|
| S/C spatial position uncertainty from TLE, | 5500 | m | R |
| OH spatial position uncertainty from GNSS/INS, | 1 | m | R |
| **Position uncertainty (random)** | **1.1** | **mrad** | **R** |

## D.3 Payload attitude uncertainty

Table D.3 - Payload attitude uncertainty

| Uncertainty contributor | Value | Unit | Type |
|---|---|---|---|
| **Nominal uncertainty [GNSS/INS]** | | | |
| Heading (azimuth) uncertainty | 2.6 | mrad | R |
| Combined pitch/roll nominal uncertainty | 1.7 | mrad | R |
| **Integration misalignment & full system absolute calibration [GNSS/INS]** | | | |
| Heading (azimuth) uncertainty | 0.05 | mrad | F |
| Combined pitch/roll uncertainty | 0.05 | mrad | F |
| **Timing & control** | 0.02 | mrad | R |
| **Payload attitude uncertainty (random)** | **3.2** | **mrad** | **R** |
| **Payload attitude uncertainty (bias)** | **1.8** | **mrad** | **F** |

## D.4 Payload pointing uncertainty

Table D.4 - Payload pointing uncertainty

| Uncertainty contributor | Value | Unit | Type |
|---|---|---|---|
| **Micro-vibrations** | 50 | µrad | R |
| **Thermoelastic effects** | 25 | µrad | F |
| **Optical window induced pointing variations** | 20 | µrad | F |
| **CPM pointing uncertainty** | | | |
| Alignment & calibration procedure uncertainty | 10 | µrad | F |
| CPA Specifications | 57.6 | µrad | R |

| | | | |
|---|---|---|---|
| **Atmospheric effects** | | | |
| Bias | 200 | µrad | F |
| Random | 200 | µrad | R |
| **Payload pointing uncertainty (random)** | **0.21** | **mrad** | **R** |
| **Payload pointing uncertainty (bias)** | **0.26** | **mrad** | **F** |

## D.5 Open-loop pointing uncertainty

Table D.5 - Open-loop pointing uncertainty

| Uncertainty contributor | Value | Unit | Type |
|---|---|---|---|
| **Payload pointing uncertainty** | | | |
| Random | 0.21 | mrad | R |
| Bias | 0.26 | mrad | F |
| **Payload attitude uncertainty** | | | |
| Random | 3.2 | mrad | R |
| Bias | 1.7 | mrad | F |
| **Position uncertainty** | | | |
| Random | 1.1 | mrad | R |
| **Total uncertainty (random)** | **3.3** | **mrad** | **R** |
| **Total uncertainty (bias)** | **2.0** | **mrad** | **F** |
| **Open-loop acquisition uncertainty** | **5.3** | **mrad** | |

## D.6 Tracking uncertainty

Table D.6 - Tracking uncertainty

| Uncertainty contributor | Value | Unit | Type |
|---|---|---|---|
| **Feedback loop uncertainty** | | | |
| **ATS feedback uncertainty** | | | |
| Calibration and alignment | 0.13 | µrad | F |
| Centroid detection uncertainty | 4.70 | µrad | R |
| **FPM actuation** | | | |

| | | | |
|---|---|---|---|
| FSM resolution | 0.1 | µrad | R |
| FSM jitter | 0.1 | µrad | R |
| CPM residual jitter | 0.14 | µrad | R |
| **External residuals** | | | |
| Local turbulence around the radome | 0.30 | µrad | R |
| Atmospheric effects | 0.30 | µrad | R |
| **Residual micro vibration** | 0.50 | µrad | R |
| **Tracking uncertainty (bias)** | 4.75 | µrad | F |
| **Tracking uncertainty (random)** | 0.98 | µrad | R |

## D.7 Point Ahead Angle (PAA) uncertainty

Table D.7 - Point Ahead Angle uncertainty

| Uncertainty contributor | Value | Unit | Type |
|---|---|---|---|
| **PAM actuation uncertainty** | | | |
| FSM accuracy (exit pupil) | 0.1 | µrad | R |
| Tx/Rx path alignment uncertainty | 0.13 | µrad | F |
| FSM resolution | 0.1 | µrad | R |
| **PAA estimation uncertainty** | 1.00 | µrad | R |
| **PAA total uncertainty (bias)** | 1.13 | µrad | F |
| **PAA total uncertainty (random)** | 0.14 | µrad | R |

# E

# UNCERTAINTY ANALYSIS AND MODELLING

## E.1 Spiral definition

This subsection intends to clarify the spiral definition used in the emulator. In practice, the spiral shape is three-dimensional. (Figure ) Each normalized point represents a cone with a given divergence extending from the OH to the infinity. The CPM angles are changed according to the equation below.

$$r = 1; \qquad \phi = \frac{spiral\ step}{2\pi} \times \theta \qquad \begin{cases} x = r\sin(\phi)\ \times \cos(\theta) \\ y = r\sin(\phi)\ \times \sin(\theta) \\ z = r\cos(\phi) \end{cases} \qquad \text{E.1}$$

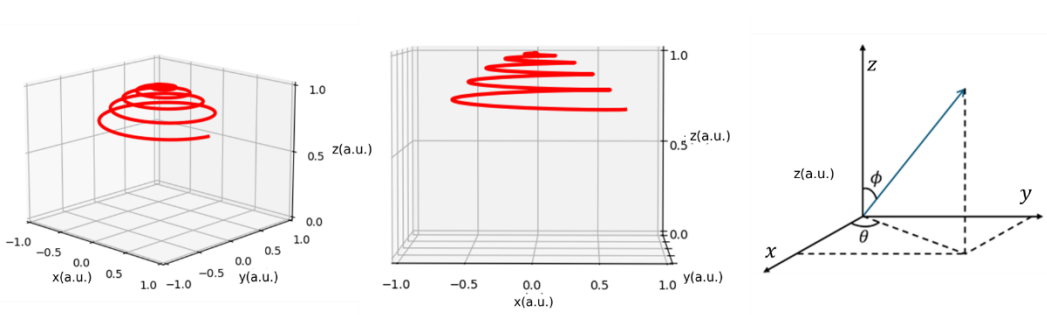


Figure E.1 - Left - 3D Spiral normalized representation;
Right - Spherical coordinates representation

However, it is a lot more intuitive and useful to represent this scan in two dimensions. Therefore, we perform one approximation that will allow to represent the scan in two dimensions. The projection of the 3D spiral to a horizontal plane is valid since the angle error is negligible (for the given FOU). Figure  illustrates both the 3D Spiral and the same projection.

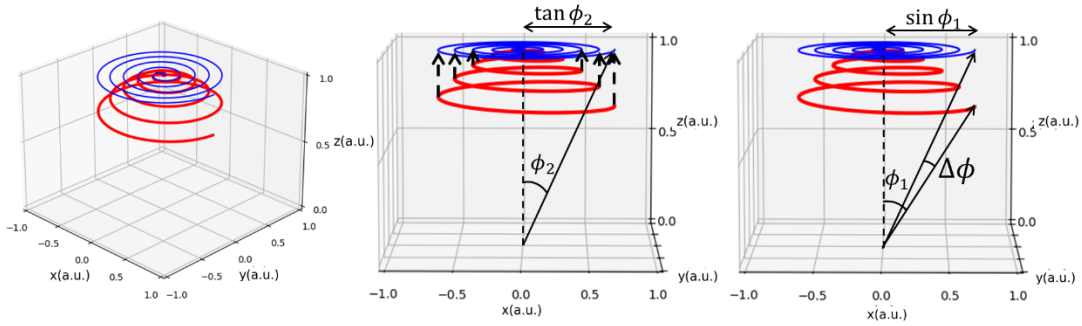


Figure E.2 - 3D Spiral projection to a horizontal plane (example)

This approximation results in a maximum error:

$$\Delta\phi = \phi_1 - \phi_2 = \\ = \phi_1 - \arctan\left(\frac{\sin\phi_1}{1}\right) \approx 10^{-7} rad \qquad 9.4$$

$$\phi_1 = FOU \approx 10^{-2} rad \qquad E.2$$

The maximum error is 5 orders of magnitude lower compared to the spiral dimension. Therefore, the horizontal projection is a valid approximation.

After the previous approximation, the three-dimensional projected spiral and the Archimedean Spiral are compared. (Figure ) The distance between any blue point and the centre of the blue spiral is given by $\tan\phi_2$. (Figure )

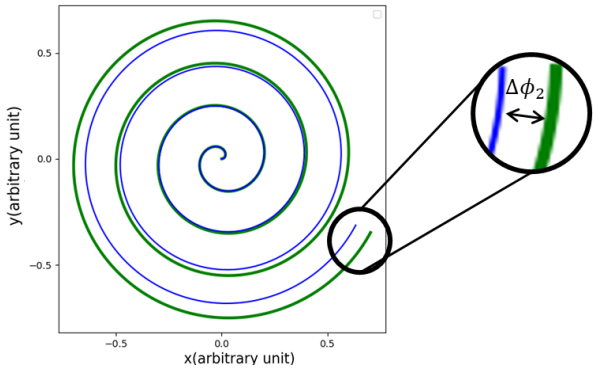


Figure E.3 - 2D Archimedean spiral vs 3D projected spiral;
Blue Spiral - 3D projected spiral; Green Spiral- 2D Archimedean spiral

Verifying the maximum error, it was concluded that the total error ($\approx 10^{-7} rad$) is negligible compared to the scan's dimension. Therefore, the scan may be represented by the Archimedean spiral equation. Although the scan is being represented in cartesian space, all distances directly correspond to angles, due to the small angle approximation

$$r \in [0, \tan FOU \approx FOU]$$

$$\theta = \frac{2\pi}{Distance_{between\ turns}} \times r \qquad 9.5$$

$$\begin{cases} x = r \times \cos\theta \ \ (m) \\ y = r \times \sin\theta \ \ (m) \end{cases} \qquad E.3$$

# E.2 Acquisition simulation diagram

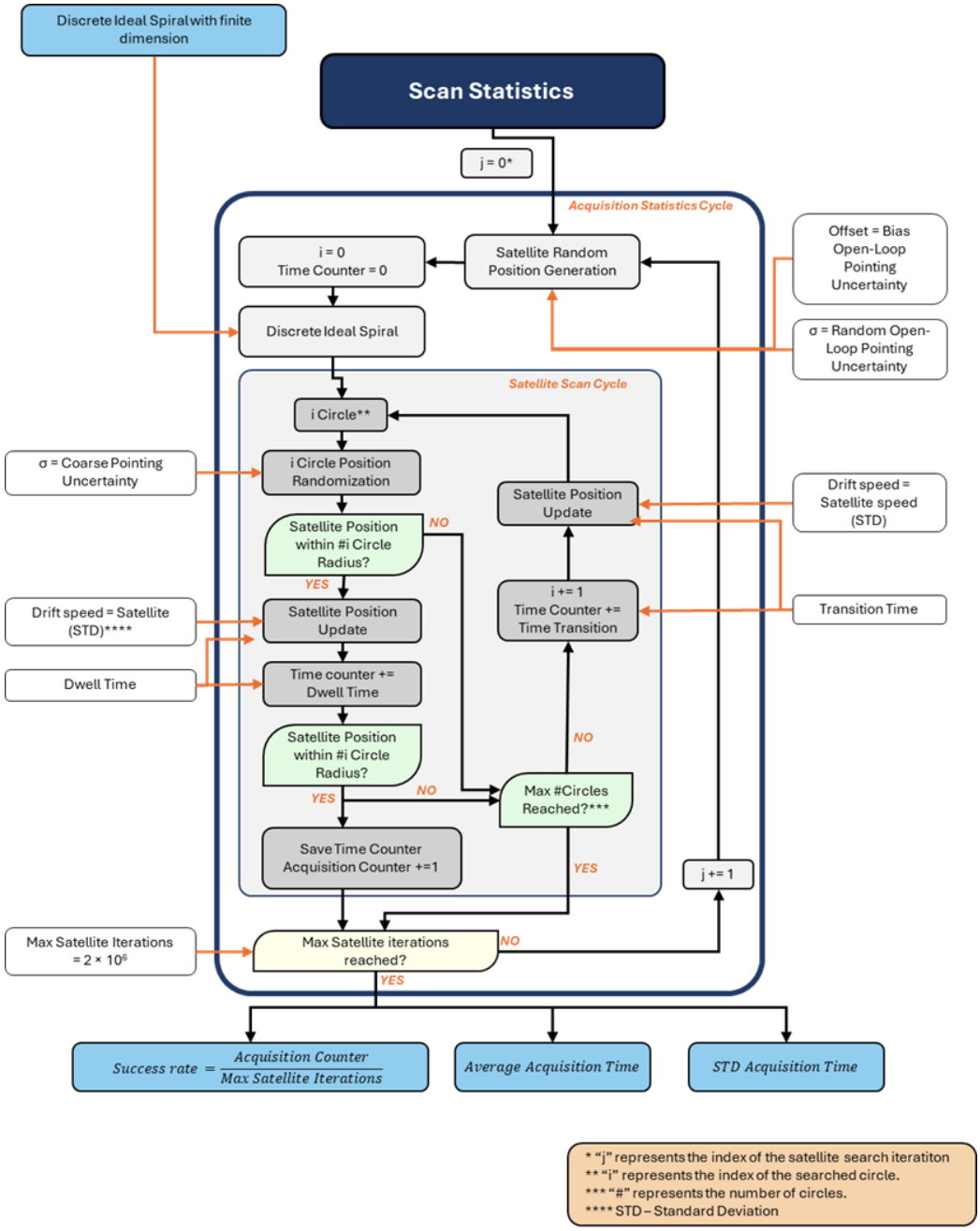


Figure E.4 - Flow diagram of the scan statistics simulation

## E.3 Speed characterization

This subsection defines the satellite's trajectory relative to the OH's frame of reference. This description will allow a more accurate approximation of the gimbal's movement along the acquisition and tracking phases (from the emulator's perspective). Although the orbits are slightly elliptical, it is correct to assume the S/C's orbit as circular with its centre coincident with Earth's centre [10].

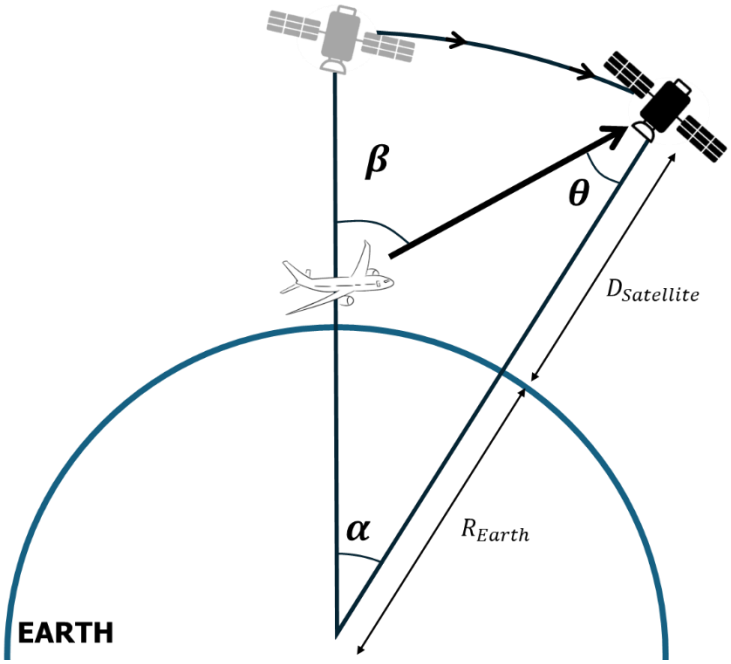


Figure E.5 - S/C's movement relative to A/C

We want to describe Beta as a function of Alpha. Looking at the triangle defined by both alpha and theta, we may apply the sines law:

$$\frac{sin(180-\beta)}{R_{Earth}+D_{Satellite}}=\frac{sin(\theta)}{R_{Earth}+D_{A/C}}$$

$$\theta=\beta-\alpha$$

$$\frac{sin(\beta)}{R_{Earth}+D_{Satellite}}=\frac{sin(\beta-\alpha)}{R_{Earth}+D_{A/C}} \qquad \text{E.4}$$

$$\frac{\sin\beta}{R_{Earth}+D_{Satellite}}=\frac{\sin\beta\cos\alpha-\cos\beta\sin\alpha}{R_{Earth}+D_{A/C}}$$

$$\beta=\arctan\frac{\sin\alpha\cdot(R_{Earth}+D_{Satellite})}{(R_{Earth}+D_{Satellite})\cdot\cos\alpha-\left(R_{Earth}+D_{A/C}\right)}$$

## E.4 Reference frame rotation

This subsection shows the multiple matrices involved in computing the scan coordinates. Using elevation and azimuth angles, the first matrix (Equation **Error! Reference source not found.**) rotates the frame reference toward the initial pointing target. In pragmatic terms, this rotation represents the pointing phase.

$$Rotation\ Matrix\ (Euler\ intrisic\ ZY) =$$
$$R_y \times R_z =$$
$$\begin{bmatrix} \cos\alpha & 0 & \sin\alpha \\ 0 & 1 & 0 \\ -\sin\alpha & 0 & \cos\alpha \end{bmatrix} \times \begin{bmatrix} \cos\gamma & -\sin\gamma & 0 \\ \sin\gamma & \cos\gamma & 0 \\ 0 & 0 & 1 \end{bmatrix} =$$
$$\begin{bmatrix} \cos\alpha\cdot\cos\gamma & -\cos\alpha\cdot\sin\gamma & 0 \\ \sin\gamma & \cos\gamma & 0 \\ -\sin\alpha\cdot\cos\gamma & \sin\alpha\cdot\cos\gamma & 1 \end{bmatrix} \quad \text{E.5}$$

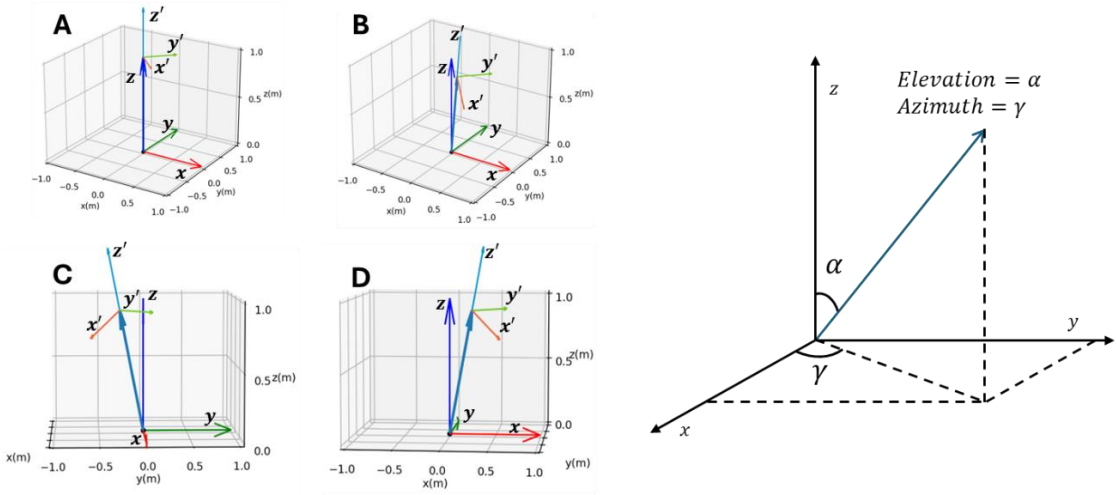


Figure E.6 - Left: Gimbal reference frame initial positions (Python emulation)
Right - Frame rotation angles represented
Azimuth rotation $= \frac{\pi}{4}$; Elevation rotation $= \frac{\pi}{8}$;
A - Azimuth rotation; B - Azimuth and elevation rotation; C - Front view; D - Side view

The acquisition phase demands the use of an uncommon matrix. The one presented below allows the CPM to rotate around an axis in the XoY plane with any angle $\theta$. (Figure ) This rotation allows the CPM to follow the predicted movement of the S/C throughout the acquisition process.

$$Rotation\ Matrix\ (Arbitrary\ axis) =$$
$$= \begin{bmatrix} \cos\alpha + \left(u_x^2\cdot(1-\cos\alpha)\right) & u_x\cdot u_y\cdot(1-\cos\alpha) & u_y\cdot\sin\alpha \\ u_y\cdot u_x\cdot(1-\cos\alpha) & \cos\alpha + \left(u_y^2\cdot(1-\cos\alpha)\right) & -u_x\cdot\sin\alpha \\ -u_y\cdot\sin\alpha & u_x\cdot\sin\alpha & \cos\alpha \end{bmatrix}; \quad \text{E.6}$$

$$u = (\cos\theta\,; \sin\theta; 0),\ u\ in\ XoY\ plane; \theta = drift\ angle + \frac{\pi}{2},$$

This rotation receives as inputs the S/C's orbital speed (translated to the A/C's reference frame through the formula present in Appendix E.3) and the predicted angle of the drift relative to the initial pointing goal's reference frame (Figure ).

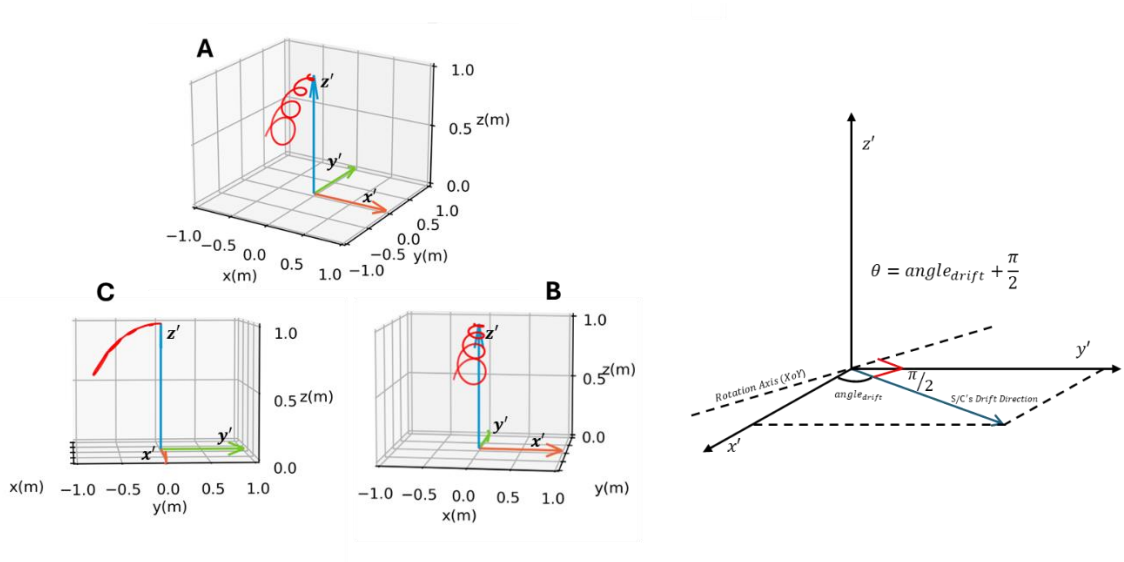


Figure E.7 - Left - Scan drift relative to the initial pointing goal's reference frame
Right - Rotation axis representation;
$Drift\ angle\ = -\frac{\pi}{2}; Azimuth\ rotation\ = -\frac{\pi}{4}; Elevation\ rotation\ = \frac{\pi}{8}$

The combination of the two previous rotations results in a model capable of describing any of the gimbals' trajectory throughout the acquisition process. Figure illustrates the combination of the two matrices referred to above.

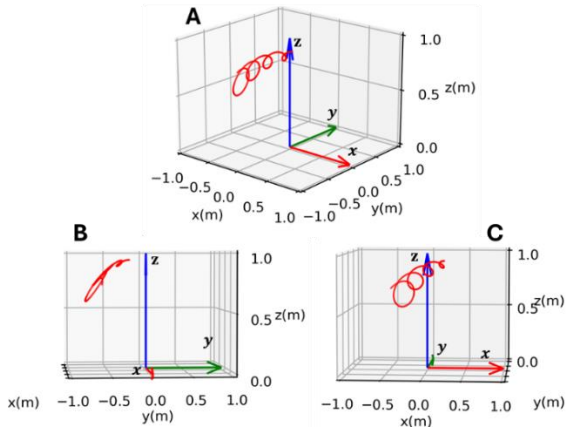


Figure E.8 - Real scan representation;
$Drift\ angle\ = -\frac{\pi}{2}; Azimuth\ rotation\ = -\frac{\pi}{4}; Elevation\ rotation\ = \frac{\pi}{8}$

# E.5 Closed-loop emulator

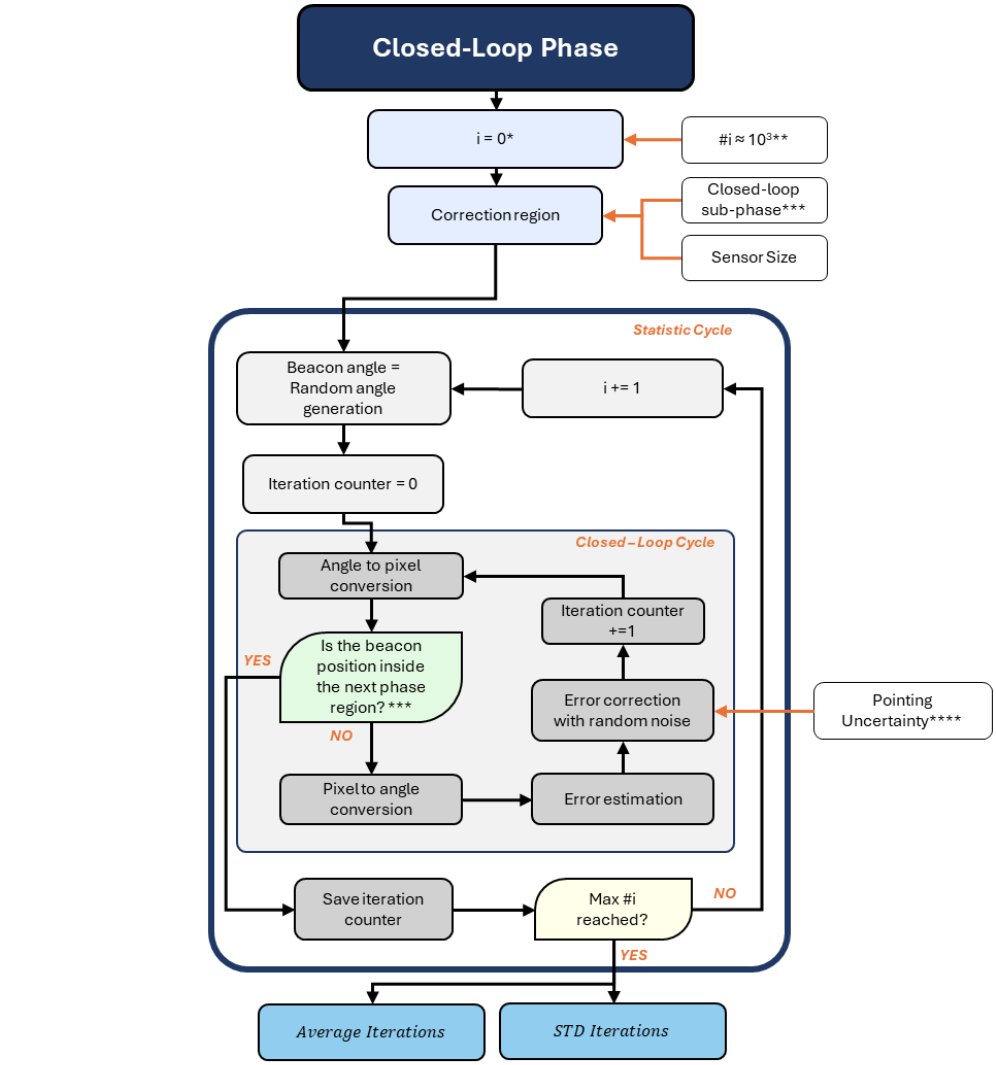


*"i" represents the index of the cycle number.
** "#" represents the numerical quantity of a certain variable
*** This diagram applies to both the Acquisition 2 and Fine Pointing Acquisition phases. The Tracking phase differs in that its loop continues as long as the communication process is active. Therefore, we analyze the system's stability during the Tracking phase, considering the relevant perturbations.
****The pointing uncertainty value is directly dependent on the current system's sub-phase.

Figure E.9 - Closed-loop emulator diagram

# F

# PERFORMANCE ANALYSIS

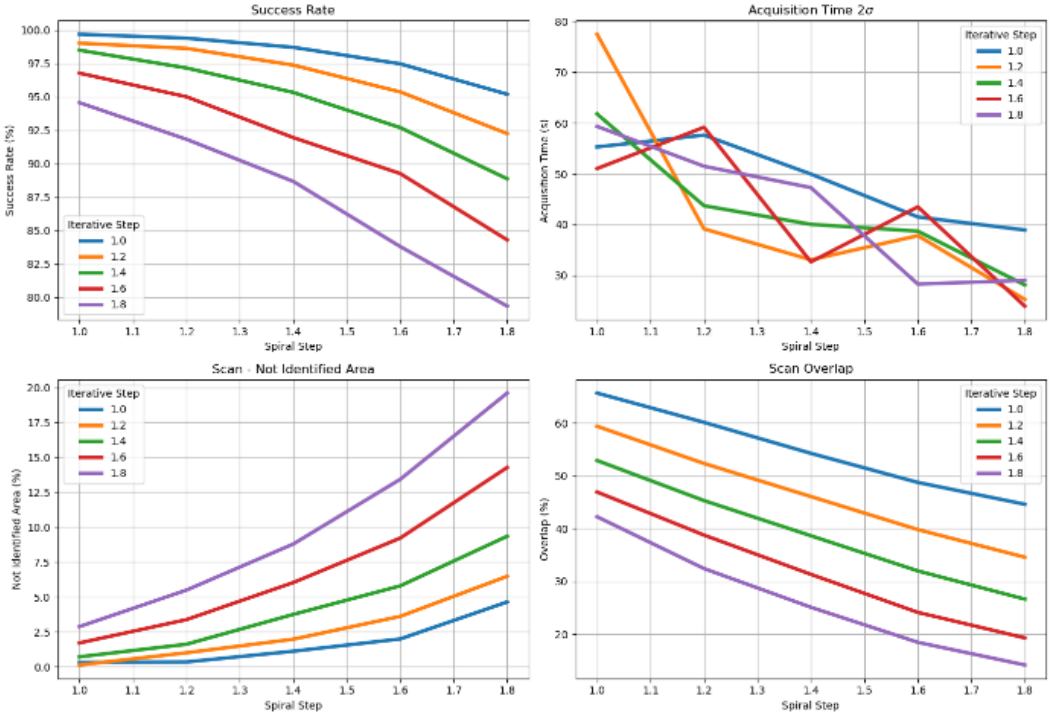


Figure F.1 - Performance analysis - 2.6 sigma

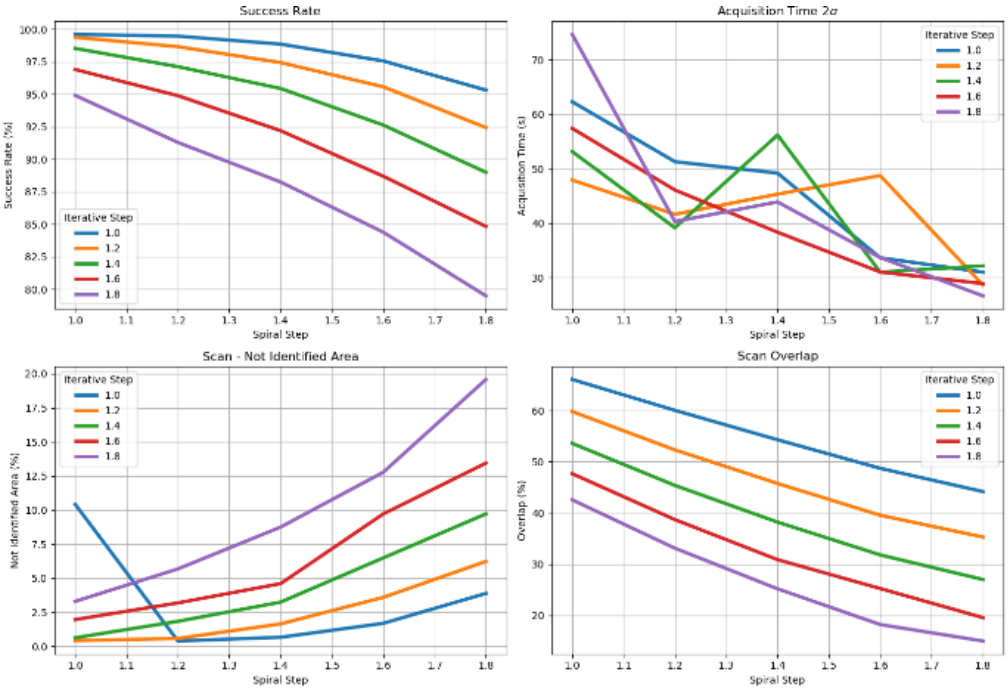


Figure F.2 - Performance analysis - 2.8 sigma